

Blackbody Simulations Report

Jason Wang^{*1}

¹The Division of Physics, Mathematics, and Astronomy, California Institute of Technology

August 19, 2025

Abstract

Blackbody radiation from warmer components surrounding cryogenic dark matter detectors can induce leakage currents and parasitic power, representing a subtle but significant source of background in rare-event searches. We first explore an analytical approach for a plane wave incident on an infinite parallel-plate waveguide. While a full solution is not obtained, we present the key governing equations and outline techniques for a complete derivation. We then develop a bounded-space, wave-based simulation that accurately captures transmission probabilities, emission locations, and outgoing wavevector distributions, enabling seamless integration with open-space, particle-like Geant4 simulations. This work provides a crucial step toward end-to-end modeling of blackbody effects, guiding both detector design optimization and predictive analyses for future dark matter experiments.

1 Introduction

Understanding and mitigating blackbody radiation effects is critical for the performance of cryogenic detectors used in rare-event searches such as dark matter detection. This paper investigates how thermal photons originating from warmer components surrounding ultra-cold detectors can impact the performance of cryogenic detectors, particularly those used in the Cryogenic Dark Matter Search (CDMS) experiment. The CDMS collaboration aims to detect weakly interacting massive particles (WIMPs), a leading dark matter candidate, using SuperCDMS detectors. These advanced detectors leverage semiconductor crystals, primarily germanium and silicon, cooled to millikelvin temperatures to measure ionization and phonon signals generated by potential dark matter interactions.

A key advantage of SuperCDMS is its enhanced shielding and low background rates, which are critical for rare-event searches. However, even with extreme cooling, a subtle but important source of background remains: blackbody radiation. While it might be expected that cooling detectors to millikelvin temperatures would suppress thermal effects, the surrounding materials such as the cryostat and electronic supports remain at higher temperatures. As demonstrated by Domange et al. (2012),¹ infrared photons from these warmer components can ionize impurity states with energy thresholds as low as 0.75 meV, corresponding to blackbody radiation at just 3.1 K. Such ionization can lead to leakage currents, which are unintended electrical currents flowing through the detectors. These interactions can pose a significant problem because the walls separating chambers of different temperatures are not entirely hermetic or sealed. Manufacturing and assembling misalignment may lead to involuntary gaps of $O(10^2 - 10^3)\mu m$ through which blackbody radiation can enter.

Photons generated by blackbody radiation spend most of their time in open space conditions, where $L \gg \lambda$ and L is the characteristic length of the space. In this regime, photons propagate in a straight-line path and can be modeled accurately as a particle. However, the propagation of photons through the non-hermetic cracks in the detector assembly means that it is important to simulate the behavior of photons in the bounded space regime as well, characterized by $\lambda \sim L$, where L is the characteristic length of the space. In this regime, photons are best modeled as waves, not particles. In the Golwala group, there is work on modeling photons in both regimes. Work in the open space regime primarily relies on Geant4, a commonly-used Monte-Carlo based particle simulator software, while work in the bounded space regime primarily relies on Ansys High Frequency Structure Simulator (HFSS), a 3d electromagnetic simulation software. By combining the open space propagation of photons in Geant4 and the

^{*}Mentored by Sunil Golwala

bounded space propagation of photons in HFSS, we will be able to build an start-to-end simulation of photons, from photon generation to photon absorption.

In this paper, we focus on modeling the propagation of photons in bounded spaces. As argued by Chang, the $O(10^2 - 10^3)\mu m$ gaps present in the mechanical design of the fridge and detector setup can be modeled as semi-open parallel-plate metallic channels in a vacuum.² While these structures are not perfectly infinite in the transverse direction, as depicted in figure 1, their $O(cm)$ length is sufficiently large that the cutoff frequency for the dominant TEM mode is effectively negligible. This absence of a cutoff allows low-frequency photons generated by blackbody sources at relatively low temperatures to propagate freely through the gaps. If a cutoff frequency were present, such radiation would be exponentially attenuated and pose no significant issue. However, the ability of these photons to propagate enables impurity site ionization via blackbody radiation, making it a credible and potentially significant source of noise that warrants careful investigation.

There are two main practical motivations for modeling the effects of blackbody radiation on dark matter detectors. First, we aim to understand the impact of blackbody-induced photoionization, particularly in the context of CDMS. While these effects have already been observed in highly sensitive transition-edge sensors (TESs), CDMS is expected to approach similar sensitivity in the future, making it increasingly important to accurately model the associated parasitic power and leakage current. To this end, we seek to perform full simulations for CDMS to quantify these effects. Secondly, we are interested in ways to mitigate the effects of such radiation by improving mechanical seals. There have been ideas ranging from adding sharp 90° turns to adding stub filters, both in an attempt to scatter the transverse electric-magnetic (TEM) mode into higher order, non-propagating modes.

The layout of the paper is as follows. In section 2, we partially solve the analytical case of plane-wave propagation through an infinite parallel-plate waveguide. While a complete solution is beyond our scope, we derive the key governing equations and provide insight into the difficulties of the problem. Then, in section 3, we streamline the simulation of incident plane waves through waveguides of arbitrary shape in HFSS. Finally, in section 4, we discuss possible improvements and future plans.

2 Analytical Solution

2.1 Infinite Parallel-Plate Waveguide Modes

In this section, we seek an analytical solution to an incoming plane wave impinging upon a crack, modeled as an infinite parallel-plate waveguide in a vacuum. The plane wave hits the crack in the $z = 0$ plane, and the waveguide axis is the $+\hat{z}$ direction. This situation is depicted in figure 1.

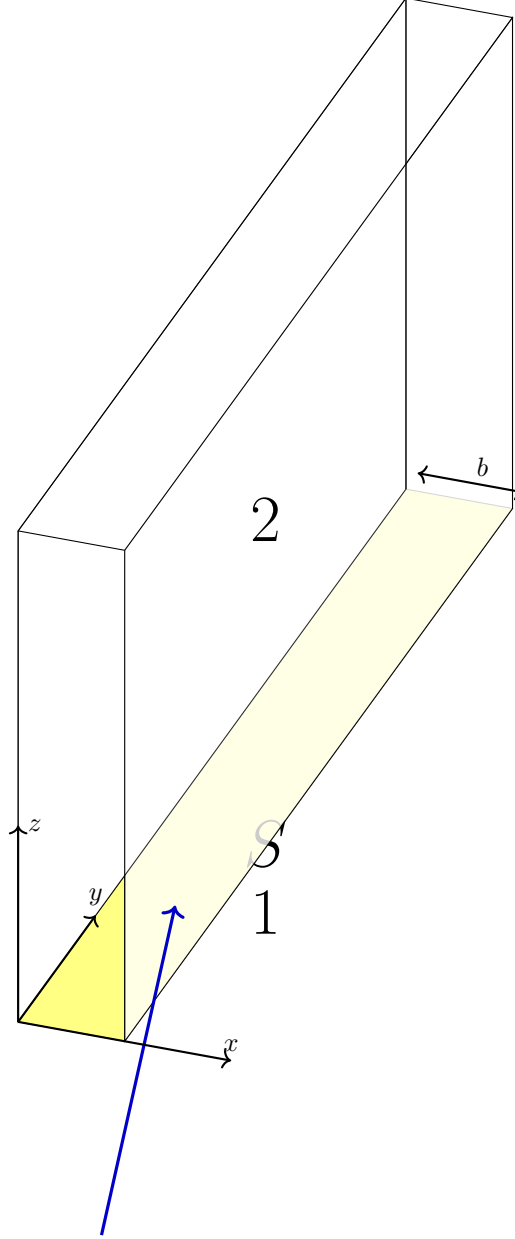


Figure 1: Diagram of a plane wave incident on a parallel-plate waveguide with the waveguide axis in the $+\hat{z}$ direction. The incoming wavevector \mathbf{k}_i is shown in blue. In the case of an infinite parallel-plate waveguide, the waveguide is infinite in the \hat{y} direction.

For future use, we write down the transverse-electric (TE) and transverse-magnetic (TM) modes of an infinite parallel-plate waveguide. Let the wavevector $\mathbf{k}_m = k_{m,x}\hat{x} + k_{m,y}\hat{y} + k_{m,z}\hat{z}$, where the subscripts m indicate that these values depend on the particular value m of interest. Because the wave still propagates in vacuum in the waveguide, and because the angular frequency is still ω , determined once and for all by the incident plane wave, we have that

$\omega = kc$ where $k = |\mathbf{k}_m|$, so in particular

$$k^2 = k_{m,x}^2 + k_{m,y}^2 + k_{m,z}^2.$$

The \hat{x} -component of the wavevector will be quantized by the boundary. Thus $k_{m,x}$ is quantized as

$$k_{m,x} = \frac{m\pi}{b}, \quad (1)$$

where m is a non-negative integer (and nonzero for TE modes), and b is the width of the crack, as shown in figure 1.

2.1.1 TE Modes

For a TE mode propagating directly into a waveguide (i.e. \mathbf{k} for that particular mode is parallel to the waveguide axis), we have that the electric field is given by

$$\mathbf{E}_m^{\text{TE}}(\mathbf{r}) = E_0 \sin(k_{m,x}x) e^{ik_{m,z}z} \hat{y},$$

but the general solution, allowing for wave propagation along any direction in the $y-z$ plane, involves rotating the coordinate system. We can parametrize this with $k_{m,y}$ and $k_{m,z}$ and write

$$\mathbf{E}_m^{\text{TE}}(\mathbf{r}) = E_0 \sin(k_{m,x}x) e^{i(k_{m,y}y + k_{m,z}z)} [k_{m,z}\hat{y} - k_{m,y}\hat{z}]. \quad (2)$$

This electric field has a component in the \hat{z} direction, which is the direction of the waveguide, so this mode is not transverse to the waveguide. It is, however, transverse to the direction of propagation, which is some direction in the $y-z$ plane parametrized by $k_{m,y}$ and $k_{m,z}$. The corresponding magnetic field can be found using $\nabla \times E = -\frac{\partial B}{\partial t}$ (the time dependence $e^{-i\omega t}$ is implied) to be

$$\mathbf{B}_m^{\text{TE}}(\mathbf{r}) = \frac{E_0}{\omega} e^{i(k_{m,y}y + k_{m,z}z)} [-(k_{m,y}^2 + k_{m,z}^2) \sin(k_{m,x}x) \hat{x} - ik_{m,x}k_{m,y} \cos(k_{m,x}x) \hat{y} - ik_{m,x}k_{m,z} \cos(k_{m,x}x) \hat{z}]. \quad (3)$$

For TE modes, $m \in \mathbb{N}$. In particular, $m = 0$ is not valid, as the associated electric field becomes 0. One can also check that the fields above satisfy all 4 of Maxwell's equations in free space ($\nabla \cdot E = 0$, $\nabla \cdot B = 0$, $\nabla \times E = -\frac{\partial B}{\partial t}$, and $\nabla \times B = \frac{1}{c^2} \frac{\partial E}{\partial t}$). These fields also satisfy the boundary conditions that the tangential components of the electric field vanish at the plate boundaries and that the normal component of the magnetic field vanishes at the plate boundaries. That is, $E_y(x=0) = E_z(x=0) = B_x(x=0) = 0$ and $E_y(x=b) = E_z(x=b) = B_x(x=b) = 0$.

For future use, note that the electric field and magnetic fields depend on y and z only through the phase factor $e^{i(k_{m,y}y + k_{m,z}z)}$, so we may factorize the electric and magnetic fields as

$$\begin{aligned} \mathbf{E}_m^{\text{TE}}(\mathbf{r}) &= \mathbf{E}_m^{\text{TE}}(x) e^{i(k_{m,y}y + k_{m,z}z)} \\ \mathbf{B}_m^{\text{TE}}(\mathbf{r}) &= \mathbf{B}_m^{\text{TE}}(x) e^{i(k_{m,y}y + k_{m,z}z)}. \end{aligned} \quad (4)$$

2.1.2 TM Modes

A similar calculation shows that for TM modes, the magnetic field is given by

$$\mathbf{B}_m^{\text{TM}}(\mathbf{r}) = B_0 \cos(k_{m,x}x) e^{i(k_{m,y}y + k_{m,z}z)} [k_{m,z}\hat{y} - k_{m,y}\hat{z}] \quad (5)$$

The corresponding electric field can be found using $\nabla \times B = \frac{1}{c^2} \frac{\partial E}{\partial t}$ to be

$$\mathbf{E}_m^{\text{TM}}(\mathbf{r}) = \frac{B_0 c^2}{\omega} e^{i(k_{m,y}y + k_{m,z}z)} [(k_{m,y}^2 + k_{m,z}^2) \cos(k_{m,x}x) \hat{x} - ik_{m,x}k_{m,y} \sin(k_{m,x}x) \hat{y} - ik_{m,x}k_{m,z} \sin(k_{m,x}x) \hat{z}]. \quad (6)$$

For TM modes $m \in \mathbb{Z}_{\geq 0}$. In particular, $m = 0$ is valid, which gives rise to a TEM mode. In this mode, the electric and magnetic fields are nonzero. We can perform the same checks and see that these fields satisfy Maxwell's equations as well as the boundary conditions of the waveguide.

As above, we may factorize the electric and magnetic fields as

$$\begin{aligned} \mathbf{E}_m^{\text{TM}}(\mathbf{r}) &= \mathbf{E}_m^{\text{TM}}(x) e^{i(k_{m,y}y + k_{m,z}z)} \\ \mathbf{B}_m^{\text{TM}}(\mathbf{r}) &= \mathbf{B}_m^{\text{TM}}(x) e^{i(k_{m,y}y + k_{m,z}z)}. \end{aligned} \quad (7)$$

2.2 Setup

The incoming plane wave enters with some angular frequency ω and some wavevector \mathbf{k}_i , which generally can be any arbitrary angle into the waveguide. The electric field $\mathbf{E}_i = E_{i,x}\hat{x} + E_{i,y}\hat{y} + E_{i,z}\hat{z}$ is perpendicular to \mathbf{k}_i , as is the magnetic field. Let us write

$$\mathbf{E}_i(\mathbf{r}) = \mathbf{E}_i e^{i\mathbf{k}_i \cdot \mathbf{r}} \quad (8)$$

where $\mathbf{k}_i = k_{i,x}\hat{x} + k_{i,y}\hat{y} + k_{i,z}\hat{z}$. Denote the magnitude of this vector $k = |\mathbf{k}_i|$, and note that the angular frequency is given as $\omega = kc$, since we are propagating in vacuum. Associated with this free-space electric field is its magnetic field, give by

$$\mathbf{B}_i(\mathbf{r}) = \frac{\hat{\mathbf{k}}_i \times \mathbf{E}_i(\mathbf{r})}{c} \quad (9)$$

The incident wave also gives rise to some transmitted wave $\mathbf{E}_t(\mathbf{r})$, which can generally be written as a sum of waveguide modes:

$$\mathbf{E}_t(\mathbf{r}) = \sum_{m=1}^{\infty} A_m^{TE} \mathbf{E}_m^{TE}(\mathbf{r}) + \sum_{m=0}^{\infty} A_m^{TM} \mathbf{E}_m^{TM}(\mathbf{r}). \quad (10)$$

Notice that the mode indices for the TE modes run from $m = 1$ to infinity, while the mode indices for TM modes run from $m = 0$ to infinity. This is because in an infinite parallel-plate waveguide, the first TM mode (which is also a TEM mode) has no cutoff frequency, while the first TE mode does. Additionally, we have included evanescent modes in this expansion, which will not ultimately contribute to the power coupled into the waveguide. Even though they rapidly decay in the waveguide, however, they are important to include for field matching. The key is that only the power coupled into the TEM mode ultimately contributes to the power coupled into the waveguide. This is because at frequency ranges of interest, as well as crack dimensions of interest, this is the only mode that can propagate through the waveguide.

2.3 Single Reflected Wave

We have thus far omitted discussion of the reflected wave(s), because the reflection behavior is far from trivial. Originally, it was inferred that the incident plane wave would give rise to just one reflected wave, with associated electric and magnetic fields given by

$$\begin{aligned} \mathbf{E}_r(\mathbf{r}) &= \mathbf{E}_r e^{i\mathbf{k}_r \cdot \mathbf{r}} \\ \mathbf{B}_r(\mathbf{r}) &= \frac{\hat{\mathbf{k}}_r \times \mathbf{E}_r(\mathbf{r})}{c} \end{aligned} \quad (11)$$

where $\mathbf{E}_r = E_{r,x}\hat{x} + E_{r,y}\hat{y} + E_{r,z}\hat{z}$ and $\mathbf{k}_r = k_{r,x}\hat{x} + k_{r,y}\hat{y} + k_{r,z}\hat{z}$. This reflected wave is constrained to the same relation $\omega = kc$, where $k = |\mathbf{k}_r|$, since it also propagates in vacuum with the same angular frequency, determined by the incoming plane wave. We shall first take a look into the consequences of the single reflected wave assumption and where it breaks down. Then, in section 2.4, we attempt to resolve the problem by accounting for a full reflected spectrum of waves.

2.3.1 Boundary Conditions

We first enumerate the various boundary conditions that will be useful in solving the problem.

Wavevector Matching At the $z = 0$ interface, the continuity of the electric field requires that

$$\begin{aligned} \mathbf{E}_i(z=0) + \mathbf{E}_r(z=0) &= \mathbf{E}_t(z=0) \\ \implies \mathbf{E}_i e^{i(k_{i,x}x + k_{i,y}y)} + \mathbf{E}_r e^{i(k_{r,x}x + k_{r,y}y)} &= \sum_{m=1}^{\infty} A_m^{TE} \mathbf{E}_m^{TE}(x) e^{ik_{m,y}y} + \sum_{m=0}^{\infty} A_m^{TM} \mathbf{E}_m^{TM}(x) e^{ik_{m,y}y}. \end{aligned} \quad (12)$$

Since this equation must hold for all y in the $z = 0$ plane (the waveguide is infinite in that direction), and the dependence on y is a simple exponential for all terms on the left and right sides of the equation, we can conclude that $k_{i,y} = k_{r,y} = k_{m,y} := k_y$ for values of m .

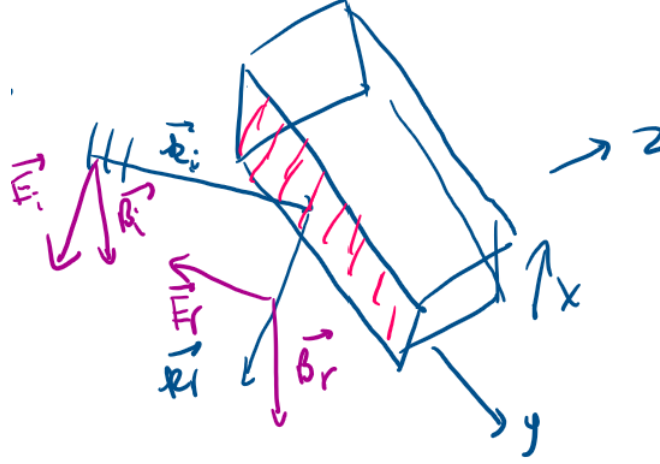


Figure 2: The incident and reflected waves associated with a plane wave excitation. The incoming wave impinges on the $x - y$ plane. We assume, for now, that the incident plane wave gives rise to only a single reflected wave. The superposition of modes excited in the waveguide is not depicted.

Regarding the \hat{x} component, we do not assume anything yet, because the waveguide is not infinite in the \hat{x} direction. To write it all out explicitly again,

$$\begin{aligned} k_{i,y} &= k_{r,y} = k_{m,y} := k_y \text{ for all } m \\ |\mathbf{k}_i| &= |\mathbf{k}_r| = |\mathbf{k}_m| = \frac{\omega}{c} := k \end{aligned} \quad (13)$$

Boundary Interface Maxwell's equations applied to the $z = 0$ interface gives 4 sets of boundary conditions, which we write out explicitly below. In the equations below, 1 and 2 refer to regions 1 and 2, as shown in figure 1.

$$\begin{aligned} \nabla \cdot E &= 0 \implies E_{\perp}^1 = E_{\perp}^2 \\ \nabla \times E &= -\frac{\partial B}{\partial t} \implies E_{\parallel}^1 = E_{\parallel}^2 \\ \nabla \cdot B &= 0 \implies B_{\perp}^1 = B_{\perp}^2 \\ \nabla \times B &= \frac{1}{c^2} \frac{\partial E}{\partial t} \implies B_{\parallel}^1 = B_{\parallel}^2 \end{aligned} \quad (14)$$

- (i) $E_{\perp}^1 = E_{\perp}^2$. Using the \hat{z} component of the electric field in equations 2 and 6, setting $z = 0$, and ignoring the $e^{ik_y y}$ component common to all fields,

$$E_{i,z} e^{ik_{i,x}x} + E_{r,z} e^{ik_{r,x}x} = -\frac{iB_0 c^2}{\omega} \sum_{m=0}^{\infty} A_m^{TM} k_{m,x} k_{m,z} \sin(k_{m,x}x) - E_0 \sum_{m=1}^{\infty} A_m^{TE} k_y \sin(k_{m,x}x) \quad (15)$$

- (ii) $E_{\parallel}^1 = E_{\parallel}^2$. Here, we have two components (\hat{x} and \hat{y}) and hence two equations. From equation 6 (there is no \hat{x} component in equation 2), the \hat{x} equation reads:

$$E_{i,x} e^{ik_{i,x}x} + E_{r,x} e^{ik_{r,x}x} = \frac{B_0 c^2}{\omega} \sum_{m=0}^{\infty} A_m^{TM} (k_y^2 + k_{m,z}^2) \cos(k_{m,x}x) \quad (16)$$

The \hat{y} equation reads (from equations 2 and 6):

$$E_{i,y} e^{ik_{i,x}x} + E_{r,y} e^{ik_{r,x}x} = -\frac{iB_0 c^2}{\omega} \sum_{m=0}^{\infty} A_m^{TM} k_{m,x} k_y \sin(k_{m,x}x) + E_0 \sum_{m=1}^{\infty} A_m^{TE} k_{m,z} \sin(k_{m,x}x) \quad (17)$$

- (iii) $B_{\perp}^1 = B_{\perp}^2$. Using the free space relationship between E and B given in equation 9 as well as the \hat{z} component of the magnetic field in equations 3 and 5, we see that

$$\left[\frac{(\hat{\mathbf{k}}_i \times \mathbf{E}_i(\mathbf{x}))_z}{c} \right] e^{ik_{i,x}x} + \left[\frac{(\hat{\mathbf{k}}_r \times \mathbf{E}_r(\mathbf{x}))_z}{c} \right] e^{ik_{r,x}x} = -B_0 \sum_{m=0}^{\infty} A_m^{TM} k_y \cos(k_{m,x}x) - \frac{iE_0}{\omega} \sum_{m=1}^{\infty} A_m^{TE} k_{m,x} k_{m,z} \cos(k_{m,x}x) \quad (18)$$

Multiplying by $k = \frac{\omega}{c}$ in the numerator and denominator of the left hand side, carrying out the cross products, using the relations given in 13, and rearranging gives

$$[k_{i,x}E_{i,y} - k_yE_{i,x}]e^{ik_{i,x}x} + [k_{r,x}E_{r,y} - k_yE_{r,x}]e^{ik_{r,x}x} = -B_0\omega \sum_{m=0}^{\infty} A_m^{TM} k_y \cos(k_{m,x}x) - iE_0 \sum_{m=1}^{\infty} A_m^{TE} k_{m,x} k_{m,z} \cos(k_{m,x}x). \quad (19)$$

- (iv) $B_{\parallel}^1 = B_{\parallel}^2$. Similar calculations and manipulations for \hat{x} and \hat{y} components of the magnetic field at the interface yields

$$[k_yE_{i,z} - k_{i,z}E_{i,y}]e^{ik_{i,x}x} + [k_yE_{r,z} - k_{r,z}E_{r,y}]e^{ik_{r,x}x} = -E_0 \sum_{m=1}^{\infty} A_m^{TE} (k_y^2 + k_{m,z}^2) \sin(k_{m,x}x) \quad (20)$$

for the \hat{x} component, and

$$[k_{i,z}E_{i,x} - k_{i,x}E_{i,z}]e^{ik_{i,x}x} + [k_{r,z}E_{r,x} - k_{r,x}E_{r,z}]e^{ik_{r,x}x} = B_0\omega \sum_{m=0}^{\infty} A_m^{TM} k_{m,z} \cos(k_{m,x}x) - iE_0 \sum_{m=1}^{\infty} A_m^{TE} k_{m,x} k_y \cos(k_{m,x}x) \quad (21)$$

for the \hat{y} component.

2.3.2 Solving the Equations

We now integrate equations 16, 19, and 21 from $x = 0$ to $x = b$. The reason we choose these 3 equations is that they include A_0^{TM} terms, and these are the only terms that remain following integration. This is because all of the cosine terms for $m \neq 0$ integrate to zero, due to typical Fourier techniques. Integrating equation 16, using the fact that only $m = 0$ remains and that $k_y^2 + k_{m=0,z}^2 = k^2 - k_{m=0,x}^2 = k^2$ gives

$$\begin{aligned} E_{i,x} \frac{e^{ik_{i,x}b} - 1}{ik_{i,x}} + E_{r,x} \frac{e^{ik_{r,x}b} - 1}{ik_{r,x}} &= \int_0^b \frac{B_0 c^2}{\omega} \sum_{m=0}^{\infty} A_m^{TM} (k_y^2 + k_{m,z}^2) \cos(k_{m,x}x) dx \\ &= \frac{B_0 c^2}{\omega} A_0^{TM} k^2 b \\ &= B_0 \omega A_0^{TM} b. \end{aligned} \quad (22)$$

Integrating equation 19 gives

$$[k_{i,x}E_{i,y} - k_yE_{i,x}] \frac{e^{ik_{i,x}b} - 1}{ik_{i,x}} + [k_{r,x}E_{r,y} - k_yE_{r,x}] \frac{e^{ik_{r,x}b} - 1}{ik_{r,x}} = -B_0 \omega A_0^{TM} k_y b. \quad (23)$$

Integrating equation 21 and using $k_{m=0,z} = \sqrt{k^2 - k_y^2 - k_{m=0,x}^2} = \sqrt{k^2 - k_y^2}$ gives

$$[k_{i,z}E_{i,x} - k_{i,x}E_{i,z}] \frac{e^{ik_{i,x}b} - 1}{ik_{i,x}} + [k_{r,z}E_{r,x} - k_{r,x}E_{r,z}] \frac{e^{ik_{r,x}b} - 1}{ik_{r,x}} = B_0 \omega A_0^{TM} \sqrt{k^2 - k_y^2} b. \quad (24)$$

The other three equations, equation 15, 17, and 20, do not contain any information about A_0^{TM} , so we proceed more generally, multiplying first by $\sin(k_n x)$, where $k_n = \frac{n\pi}{b}$ and $n \in \mathbb{N}$, and then integrating from $x = 0$ to $x = b$. The orthogonality of the sine functions corresponding to different values of n means that only the $m = n$ terms remain in the summation. Also, $\int_0^b \sin^2(k_n x) dx = \frac{b}{2}$. Then, equation 15 yields

$$E_{i,z} \int_0^b \sin\left(\frac{n\pi x}{b}\right) e^{ik_{i,x}x} dx + E_{r,z} \int_0^b \sin\left(\frac{n\pi x}{b}\right) e^{ik_{r,x}x} dx = -\frac{iB_0 c^2}{\omega} (A_n^{TM} \frac{n\pi}{b} k_{n,z} \frac{b}{2}) - E_0 A_n^{TE} k_y \frac{b}{2}. \quad (25)$$

Similarly, integrating equation 17 with respect to the sine yields

$$E_{i,y} \int_0^b \sin\left(\frac{n\pi x}{b}\right) e^{ik_{i,x}x} dx + E_{r,y} \int_0^b \sin\left(\frac{n\pi x}{b}\right) e^{ik_{r,x}x} dx = -\frac{iB_0 c^2}{\omega} (A_n^{TM} \frac{n\pi}{b} k_y \frac{b}{2}) + E_0 A_n^{TE} k_{n,z} \frac{b}{2}. \quad (26)$$

Finally, integrating equation 20 with respect to the sine yields

$$[k_y E_{i,z} - k_{i,z} E_{i,y}] \int_0^b \sin\left(\frac{n\pi x}{b}\right) e^{ik_{i,x}x} dx + [k_y E_{r,z} - k_{r,z} E_{r,y}] \int_0^b \sin\left(\frac{n\pi x}{b}\right) e^{ik_{r,x}x} dx = -E_0 A_n^{TE} (k^2 - (\frac{n\pi}{b})^2) \frac{b}{2}. \quad (27)$$

Multiplying equation 25 by k_y and equation 26 by $k_{n,z}$ and subtracting gives

$$[k_y E_{i,z} - k_{n,z} E_{i,y}] \int_0^b \sin\left(\frac{n\pi x}{b}\right) e^{ik_{i,x}x} dx + [k_y E_{r,z} - k_{n,z} E_{r,y}] \int_0^b \sin\left(\frac{n\pi x}{b}\right) e^{ik_{r,x}x} dx = -E_0 A_n^{TE} \frac{b}{2} (k_y^2 + k_{n,z}^2). \quad (28)$$

But $k_y^2 + k_{n,z}^2 = k^2 - k_{n,x}^2$, and so by comparing equations 27 and 28, we find that

$$E_{i,y} [k_{n,z} - k_{i,z}] \int_0^b \sin\left(\frac{n\pi x}{b}\right) e^{ik_{i,x}x} dx = E_{r,y} [k_{r,z} - k_{n,z}] \int_0^b \sin\left(\frac{n\pi x}{b}\right) e^{ik_{r,x}x} dx. \quad (29)$$

Importantly, this holds for all values of $n \in \mathbb{N}$. As n varies, $k_{n,z}$ changes, as does the value of each integral, but this equality is maintained regardless of the value of n . There are two ways this may occur. One possibility is that $E_{i,y} = 0$ and $E_{r,y} = 0$. In the general case where the electric field of the incoming wave is in an arbitrary direction, however, the only way this equality can occur is if $E_{i,y} = -E_{r,y}$, $k_{r,x} = k_{i,x}$, and $k_{r,z} = k_{i,z}$.

Plugging this result back into 22, 23, and 24 and using the relations described, we see that

$$\begin{aligned} (E_{i,x} + E_{r,x}) \frac{e^{ik_{i,x}b} - 1}{ik_{i,x}} &= B_0 \omega A_0^{TM} b \\ (-k_y E_{i,x} - k_y E_{r,x}) \frac{e^{ik_{i,x}b} - 1}{ik_{i,x}} &= -B_0 \omega A_0^{TM} k_y b \\ (k_{i,z} E_{i,x} - k_{i,x} E_{i,z} - k_{i,z} E_{r,x} - k_{i,x} E_{r,z}) \frac{e^{ik_{i,x}b} - 1}{ik_{i,x}} &= B_0 \omega A_0^{TM} \sqrt{k^2 - k_y^2} b \end{aligned} \quad (30)$$

As expected, the first and second equations are now identical. Combining these equations with $\mathbf{k}_r \cdot \mathbf{E}_r = k_{r,x} E_{r,x} + k_{r,y} E_{r,y} + k_{r,z} E_{r,z} = k_{i,x} E_{r,x} - k_y E_{i,y} + k_{i,z} E_{r,z} = 0$ yields a system of 3 independent equations in 3 variables: $E_{r,x}$, $E_{r,z}$, and A_0^{TM} . Solving, we find that $E_{r,x} = -E_{i,x}$, $E_{r,z} = -E_{i,z}$, and $A_0^{TM} = 0$.

The result hence ends up unsatisfactorily being a rather trivial solution:

$$\begin{aligned} k_{r,x} &= k_{i,x}; k_{r,y} = k_{i,y}; k_{r,z} = k_{i,z} \\ E_{r,x} &= -E_{i,x}; E_{r,y} = -E_{i,y}; E_{r,z} = -E_{i,z} \\ A_0^{TM} &= 0. \end{aligned} \quad (31)$$

Although this is mathematically a solution to the above system, it is unphysical. For the general case of arbitrary \mathbf{k}_i and perpendicular \mathbf{E}_i , the solution corresponds to a solution where the reflected plane wave is not in fact reflected, but rather persists into the waveguide, with its \mathbf{k} vector unchanged and all \mathbf{E} fields flipped. Mathematically, this works out because the field at the $z = 0$ plane is then zero, and so no modes need to be excited for the boundary conditions to work out. However, physically we know that this does not happen, and the reflected wave is reflected backward, not into the waveguide.

Even for the case of normal incidence, where $k_{i,x} = k_{i,y} = 0$, we are no longer guaranteed a solution. Besides the mathematical derivation above, we can reason to this result as follows. Because incidence is normal, $B_{i,z} = 0$, since the magnetic field is perpendicular to the wavevector (the reflected field will also have $k_{r,x} = k_{r,y} = 0$ by symmetry, and hence $B_{r,z} = 0$ as well). For $k_y = 0$, the magnetic field for the TM mode (equation 5) is entirely in the \hat{y} direction, so the sum of the magnetic fields of the TE modes excited must match $B_{i,z} = 0$. However, such a Fourier sum is zero only if all of its coefficients are zero, and hence $A_n^{TE} = 0$ for all n . The \hat{y} continuity equation for the electric field (equation 17) then reads $E_{i,y} + E_{r,y} = 0$, and the \hat{x} continuity equation for the magnetic field (equation

20) reads $-k_{i,z}E_{i,y} - k_{r,z}E_{r,y} = 0$, which implies that either (1) $E_{r,y} = E_{i,y} = 0$, or (2) $E_{r,y} = -E_{i,y}$ and $k_{i,z} = k_{r,z}$. That is, we have again reached the unphysical solution.

At normal incidence, there is a valid solution when $\mathbf{E}_i = E_{i,x}\hat{x}$, which couples entirely into the TEM mode. This is because in this case, $E_{i,y} = E_{r,y} = 0$, which automatically solves equation 29. There is then no restriction that $k_{r,z} = k_{i,z}$, and in fact in this case $\mathbf{E}_r = 0$, and the incoming wave couples completely into the waveguide.

Another way to think about it is that at $x = 0$ and $x = b$, our TM and TE modes have no \hat{y} -component, while an arbitrary incoming electric field can have an $E_{i,y}$ component. Thus it is impossible to have a component of E along the \hat{y} direction at $x = 0$ and $x = b$, and hence the TE and TM modes in the waveguide combined cannot satisfy this boundary condition.

2.4 Adding a Reflected Spectrum

In view of the analysis above, we conclude that it is impossible that given a plane wave incident at some arbitrary angle, the reflected wave consists of just a single plane wave. Instead, there must be a spectrum of reflected waves, as is typical for plane wave diffraction. There have been a variety of efforts in solving similar problems via the Wiener-Hopf method, mode matching procedures, and hybrid combinations of ray and modal techniques.³ However, many of these techniques are used in slightly different contexts. Collins, for example, uses the Wiener-Hopf method to solve the case of a plane wave incident on an infinite array of parallel equispaced metallic plates, which satisfy periodic boundary conditions.⁴ Koshikawa and Kobayashi perform an analysis on a planar terminated cavity with material loading, where they also saw a spectrum of scattered fields.⁵ Because our setup differs in important ways from these prior works, we adopt an alternative approach inspired by section 2.3. Although we do not arrive at a complete analytical solution, we make substantial progress. Our results lay the groundwork for future efforts, which may ultimately yield a closed-form solution using more advanced tools such as the Wiener-Hopf method.

In section 2.3, we concluded that we cannot write the reflected wave as a single wave as in equation 11. Instead, we should write the reflected wave as a superposition of reflected waves:

$$\mathbf{E}_r(\mathbf{r}) = \int_{-\infty}^{\infty} \tilde{\mathbf{E}}_r(k_x) e^{i\mathbf{k}\cdot\mathbf{r}} dk_x, \quad (32)$$

which is in effect a Fourier transform over the reflected electric field. Notice that we integrate only over k_x ; this is because, as argued before, k_y remains the same for the incident, transmitted, and all reflected waves. For the reflected wave $\mathbf{k} = (k_x, k_y, k_z)$, k_z is then given by $k_z = -\sqrt{\left(\frac{\omega}{c}\right)^2 - k_x^2 - k_y^2}$, since each reflected wave is still constrained to have $|\mathbf{k}|^2 = k_x^2 + k_y^2 + k_z^2$ and by definition, a reflected wave satisfies $k_z < 0$.

2.4.1 Field Expressions

For completeness, we provide the expressions for the electric and magnetic fields in the two regions. Since we are focused on matching the boundary conditions at $z = 0$, the fields below are written in the limit as $z \rightarrow 0$.

- **Region 1** ($z < 0$): Free space. The electric fields look like

$$\begin{aligned} \mathbf{E}_i(x, y, 0) &= \mathbf{E}_i e^{i(k_{i,x}x + k_y y)} \\ \mathbf{E}_r(x, y, 0) &= \int_{-\infty}^{\infty} \tilde{\mathbf{E}}_r(k_x) e^{i(k_x x + k_y y)} dk_x, \end{aligned} \quad (33)$$

Thus, the total electric field in region 1 looks like

$$\mathbf{E}_1(x, y, 0) = \left[\mathbf{E}_i e^{ik_{i,x}x} + \int_{-\infty}^{\infty} \tilde{\mathbf{E}}_r(k_x) e^{ik_x x} dk_x \right] e^{ik_y y}. \quad (34)$$

The associated magnetic field is

$$\mathbf{B}_1(x, y, 0) = \left[\mathbf{B}_i e^{ik_{i,x}x} + \int_{-\infty}^{\infty} \tilde{\mathbf{B}}_r(k_x) e^{ik_x x} dk_x \right] e^{ik_y y}. \quad (35)$$

where $\mathbf{B}_i = \frac{\hat{\mathbf{k}}_i \times \mathbf{E}_i}{c}$ and $\tilde{\mathbf{B}}_r(k_x) = \frac{\hat{\mathbf{k}}(k_x) \times \tilde{\mathbf{E}}_r(k_x)}{c}$. Note that we have defined $\hat{\mathbf{k}}(k_x)$ to be the unit vector in the direction parametrized by k_x , i.e. $\hat{\mathbf{k}}(k_x) = \frac{\mathbf{k}}{|\mathbf{k}|}$ where $k = (k_x, k_y, -\sqrt{k^2 - k_x^2 - k_y^2})$.

- **Region 2** ($z > 0$): Parallel-plate waveguide. The electric field is simply the sum of all the waveguide modes excited, i.e.

$$\mathbf{E}_2(x, y, 0) = \sum_{m=1}^{\infty} A_m^{TE} \mathbf{E}_m^{TE}(x) e^{ik_y y} + \sum_{m=0}^{\infty} A_m^{TM} \mathbf{E}_m^{TM}(x) e^{ik_y y} \quad (36)$$

where we have made use of the decomposition in equations 4 and 7. Similarly,

$$\mathbf{B}_2(x, y, 0) = \sum_{m=1}^{\infty} A_m^{TE} \mathbf{B}_m^{TE}(x) e^{ik_y y} + \sum_{m=0}^{\infty} A_m^{TM} \mathbf{B}_m^{TM}(x) e^{ik_y y}. \quad (37)$$

2.4.2 Boundary Conditions

The boundary conditions are identical to those discussed in section 2.3.1: all components of the electric and magnetic fields should be continuous. Thus, matching the fields given above and canceling out a common component of $e^{ik_y y}$, we arrive at

$$\mathbf{E}_i e^{ik_{i,x} x} + \int_{-\infty}^{\infty} \tilde{\mathbf{E}}_r(k_x) e^{ik_x x} dk_x = \sum_{m=1}^{\infty} A_m^{TE} \mathbf{E}_m^{TE}(x) + \sum_{m=0}^{\infty} A_m^{TM} \mathbf{E}_m^{TM}(x) \quad (38)$$

$$\mathbf{B}_i e^{ik_{i,x} x} + \int_{-\infty}^{\infty} \tilde{\mathbf{B}}_r(k_x) e^{ik_x x} dk_x = \sum_{m=1}^{\infty} A_m^{TE} \mathbf{B}_m^{TE}(x) + \sum_{m=0}^{\infty} A_m^{TM} \mathbf{B}_m^{TM}(x). \quad (39)$$

2.4.3 Solving the Equations

To solve these equations, we make abundant use of orthogonality. In fact, we claim that for the electric and magnetic fields for the TM and TE modes given in equations 2, 3, 6, and 5, the following relations are satisfied:

$$\begin{aligned} \int_0^b \mathbf{E}_\alpha^{\mathbf{TX}_1}(x) \cdot \mathbf{E}_\beta^{\mathbf{TX}_2}(x) dx &\propto \delta_{\alpha,\beta} \delta_{TX_1, TX_2} \\ \int_0^b \mathbf{B}_\alpha^{\mathbf{TX}_1}(x) \cdot \mathbf{B}_\beta^{\mathbf{TX}_2}(x) dx &\propto \delta_{\alpha,\beta} \delta_{TX_1, TX_2}. \end{aligned} \quad (40)$$

where here δ refers to the Kronecker delta function. These relations are quite easily proven directly by checking the equations above, or alternatively via the orthogonality of EM modes in a waveguide. This is entirely analogous to the orthogonality arguments used in the case of a single reflected plane wave, but written in more general terms.

Then, dotting equation 38 with $\mathbf{E}_n^{\mathbf{TE}}(x)$ and integrating from $x = 0$ to $x = b$ gives

$$\int_0^b \mathbf{E}_i \cdot \mathbf{E}_n^{\mathbf{TE}}(x) e^{ik_{i,x} x} dx + \int_0^b \mathbf{E}_n^{\mathbf{TE}}(x) \cdot \left[\int_{-\infty}^{\infty} \tilde{\mathbf{E}}_r(k_x) e^{ik_x x} dk_x \right] dx = \int_0^b \mathbf{E}_n^{\mathbf{TE}}(x) \cdot \left[\sum_{m=1}^{\infty} A_m^{TE} \mathbf{E}_m^{\mathbf{TE}}(x) + \sum_{m=0}^{\infty} A_m^{TM} \mathbf{E}_m^{\mathbf{TM}}(x) \right] dx \quad (41)$$

Using the orthogonality of modes described above, the right hand side simplifies to $A_n^{TE} \int_0^b |\mathbf{E}_n^{\mathbf{TE}}(x)|^2 dx$, and using our expression for the electric field of TE modes given in equation 2, we can compute the right-hand side explicitly to be

$$A_n^{TE} \int_0^b |\mathbf{E}_n^{\mathbf{TE}}(x)|^2 dx = A_n^{TE} \frac{b}{2} E_0^2 (k^2 - k_{n,x}^2). \quad (42)$$

Thus, we conclude that

$$A_n^{TE} = \frac{2}{b E_0^2 (k^2 - k_{n,x}^2)} \left(\int_0^b \mathbf{E}_i \cdot \mathbf{E}_n^{\mathbf{TE}}(x) e^{ik_{i,x} x} dx + \int_0^b \mathbf{E}_n^{\mathbf{TE}}(x) \cdot \left[\int_{-\infty}^{\infty} \tilde{\mathbf{E}}_r(k_x) e^{ik_x x} dk_x \right] dx \right) \quad (43)$$

We could have also determined the coefficient A_n^{TE} via equation 39, the continuity equation for the magnetic field. The resulting form is different, but the result must hold for all n . This then implies that whatever the final result for $\tilde{\mathbf{E}}_r(k_x)$, it must satisfy a certain relation between E and B .

To find A_n^{TM} , we proceed analogously to find the result

$$A_n^{TM} = \begin{cases} \frac{2}{bB_0^2 c^2 (k^2 - k_{n,x}^2)} \left(\int_0^b \mathbf{E}_i \cdot \mathbf{E}_n^{\text{TM}}(x) e^{ik_{i,x}x} dx + \int_0^b \mathbf{E}_n^{\text{TM}}(x) \cdot \left[\int_{-\infty}^{\infty} \tilde{\mathbf{E}}_r(k_x) e^{ik_x x} dk_x \right] dx \right) & \text{for } n > 0 \\ \frac{1}{bB_0^2 c^2 k^2} \left(\int_0^b \mathbf{E}_i \cdot \mathbf{E}_0^{\text{TM}}(x) e^{ik_{i,x}x} dx + \int_0^b \mathbf{E}_0^{\text{TM}}(x) \cdot \left[\int_{-\infty}^{\infty} \tilde{\mathbf{E}}_r(k_x) e^{ik_x x} dk_x \right] dx \right) & \text{for } n = 0 \end{cases} \quad (44)$$

Notice that in the case of A_n^{TM} , we split into $n > 0$ and $n = 0$ cases. The reason behind this is the same as how in the typical formulation of Fourier series, the offset term has an additional factor of 2.

For future use, we will rewrite the expressions for A_n^{TE} and A_n^{TM} in a different form. Firstly, we rename $k_x \rightarrow k'_x$ and interchange the order of integration in order to arrive at

$$\begin{aligned} A_n^{TE} &= \frac{2}{bE_0^2 (k^2 - k_{n,x}^2)} \left(\int_0^b \mathbf{E}_i \cdot \mathbf{E}_n^{\text{TE}}(x) e^{ik_{i,x}x} dx + \int_{-\infty}^{\infty} \tilde{\mathbf{E}}_r(k'_x) \cdot \left[\int_0^b \mathbf{E}_n^{\text{TE}}(x) e^{ik'_x x} dx \right] dk'_x \right) \\ A_n^{TM} &= \begin{cases} \frac{2}{bB_0^2 c^2 (k^2 - k_{n,x}^2)} \left(\int_0^b \mathbf{E}_i \cdot \mathbf{E}_n^{\text{TM}}(x) e^{ik_{i,x}x} dx + \int_{-\infty}^{\infty} \tilde{\mathbf{E}}_r(k'_x) \cdot \left[\int_0^b \mathbf{E}_n^{\text{TM}}(x) e^{ik'_x x} dx \right] dk'_x \right) & \text{for } n > 0 \\ \frac{1}{bB_0^2 c^2 k^2} \left(\int_0^b \mathbf{E}_i \cdot \mathbf{E}_0^{\text{TM}}(x) e^{ik_{i,x}x} dx + \int_{-\infty}^{\infty} \tilde{\mathbf{E}}_r(k'_x) \cdot \left[\int_0^b \mathbf{E}_0^{\text{TM}}(x) e^{ik'_x x} dx \right] dk'_x \right) & \text{for } n = 0 \end{cases} \end{aligned} \quad (45)$$

Let us define the auxiliary functions

$$\begin{aligned} \tilde{\mathbf{E}}_n^{\text{TE}}(k_x) &= \int_0^b \mathbf{E}_n^{\text{TE}}(x) e^{-ik_x x} dx \\ \tilde{\mathbf{E}}_n^{\text{TM}}(k_x) &= \int_0^b \mathbf{E}_n^{\text{TM}}(x) e^{-ik_x x} dx \\ I_n^{TE} &= \frac{2}{bE_0^2 (k^2 - k_{n,x}^2)} \int_0^b \mathbf{E}_i \cdot \mathbf{E}_n^{\text{TE}}(x) e^{ik_{i,x}x} dx \\ I_n^{TM} &= \begin{cases} \frac{2}{bE_0^2 (k^2 - k_{n,x}^2)} \int_0^b \mathbf{E}_i \cdot \mathbf{E}_n^{\text{TM}}(x) e^{ik_{i,x}x} dx & \text{for } n > 0 \\ \frac{1}{bE_0^2 k^2} \int_0^b \mathbf{E}_i \cdot \mathbf{E}_0^{\text{TM}}(x) e^{ik_{i,x}x} dx & \text{for } n = 0 \end{cases} \\ \tilde{\mathbf{K}}_n^{\text{TE}}(k_x) &= \frac{2}{bE_0^2 (k^2 - k_{n,x}^2)} \tilde{\mathbf{E}}_n^{\text{TE}}(k_x) \\ \tilde{\mathbf{K}}_n^{\text{TM}}(k_x) &= \begin{cases} \frac{2}{bB_0^2 c^2 (k^2 - k_{n,x}^2)} \tilde{\mathbf{E}}_n^{\text{TM}}(k_x) & \text{for } n > 0 \\ \frac{1}{bB_0^2 c^2 k^2} \tilde{\mathbf{E}}_0^{\text{TM}}(k_x) & \text{for } n = 0. \end{cases} \end{aligned} \quad (46)$$

The reason we define these functions is to be able to write A_n^{TE} and A_n^{TM} in a more concise fashion. Additionally, all of these functions are known functions of \mathbf{E}_i and k_x , so in principle they are well-determined. Using these functions, we may rewrite

$$\begin{aligned} A_n^{TE} &= I_n^{TE} + \int_{-\infty}^{\infty} \tilde{\mathbf{E}}_r(k'_x) \cdot \tilde{\mathbf{K}}_n^{\text{TE}}(-k'_x) dk'_x \\ A_n^{TM} &= I_n^{TM} + \int_{-\infty}^{\infty} \tilde{\mathbf{E}}_r(k'_x) \cdot \tilde{\mathbf{K}}_n^{\text{TM}}(-k'_x) dk'_x. \end{aligned} \quad (47)$$

We are most interested in the spectrum $\tilde{\mathbf{E}}_r(k_x)$. Knowing this spectrum would allow us to plug back into equations 43 and 44 to find the coefficients A_n^{TE} and A_n^{TM} , which give the coupling coefficients into the various modes. In order to do so, we perform a Fourier-like transform in x on equation 38, the continuity equation for the electric field; the only difference is that instead of integrating from $(-\infty, \infty)$, we integrate from $[0, b]$ due to the physical constraints of the problem. This results in

$$\begin{aligned} \mathbf{E}_i \int_0^b e^{-ik_x x} e^{ik_{i,x}x} dx + \int_0^b e^{-ik_x x} \left[\int_{-\infty}^{\infty} \tilde{\mathbf{E}}_r(k'_x) e^{ik'_x x} dk'_x \right] dx &= \sum_{m=1}^{\infty} A_m^{TE} \int_0^b \mathbf{E}_m^{\text{TE}}(x) e^{-ik_x x} dx + \sum_{m=0}^{\infty} A_m^{TM} \int_0^b \mathbf{E}_m^{\text{TM}}(x) e^{-ik_x x} dx \\ \Rightarrow \mathbf{E}_i \frac{e^{i(k_{i,x} - k_x)b} - 1}{i(k_{i,x} - k_x)} + \int_{-\infty}^{\infty} \tilde{\mathbf{E}}_r(k'_x) \frac{e^{i(k'_x - k_x)b} - 1}{i(k'_x - k_x)} dk'_x &= \sum_{m=1}^{\infty} A_m^{TE} \tilde{\mathbf{E}}_m^{\text{TE}}(k_x) + \sum_{m=0}^{\infty} A_m^{TM} \tilde{\mathbf{E}}_m^{\text{TM}}(k_x) \end{aligned} \quad (48)$$

Let us also further define the known functions

$$\begin{aligned}\tilde{\mathbf{G}}(k_x) &= \mathbf{E}_i \frac{e^{i(k_{i,x}-k_x)b} - 1}{i(k_{i,x} - k_x)} \\ \tilde{\psi}(k_x) &= \tilde{\mathbf{G}}(k_x) - \sum_{n=1}^{\infty} I_n^{TE} \tilde{\mathbf{E}}_n^{TE}(k_x) - \sum_{n=0}^{\infty} I_n^{TM} \tilde{\mathbf{E}}_n^{TM}(k_x).\end{aligned}\tag{49}$$

Then, plugging in the expressions from equations 47 into equation 48 simplifies the electric field continuity equation into

$$\tilde{\psi}(k_x) + \int_{-\infty}^{\infty} \tilde{\mathbf{E}}_r(k'_x) \frac{e^{i(k'_x-k_x)b} - 1}{i(k'_x - k_x)} dk'_x - \sum_{m=1}^{\infty} \tilde{\mathbf{E}}_m^{TE}(k_x) \int_{-\infty}^{\infty} \tilde{\mathbf{E}}_r(k'_x) \cdot \tilde{\mathbf{K}}_m^{TE}(-k'_x) dk'_x - \sum_{m=0}^{\infty} \tilde{\mathbf{E}}_m^{TM}(k_x) \int_{-\infty}^{\infty} \tilde{\mathbf{E}}_r(k'_x) \cdot \tilde{\mathbf{K}}_m^{TM}(-k'_x) dk'_x = 0.\tag{50}$$

This equality must hold regardless of the value of k_x used in the transform. As mentioned previously, it is possible that this equation admits an analytical solution via Wiener-Hopf techniques. Alternatively, the $\tilde{\mathbf{E}}_m^{TE}(k'_x)$ values may be estimated numerically by choosing various different values of k_x and finding a spectrum of $\tilde{\mathbf{E}}_m^{TE}(k'_x)$ that simultaneously satisfies equation 50 for all such k_x . Finally, once reasonable values of $\tilde{\mathbf{E}}_m^{TE}(k'_x)$ are obtained, we allow plug back into equations 43 and 44 to find the coefficients A_n^{TE} and A_n^{TM} , giving us the coupling coefficients for the various modes.

2.4.4 Case study: Normal Incidence, TEM Mode

For this case study, we assume that incident plane wave hits the $z = 0$ plane at normal incidence, meaning $k_{i,x} = k_{i,y} = 0$ and $k_{i,z} = k$. We also assume that it is TM polarized, and so $E_{i,y} = 0$.

Because this particular initial wave exhibits perfect transmission, we expect $\tilde{\mathbf{E}}_r(k_x) = 0$ for all k_x ; that is, there is no reflected wave. This, combined with equation 47, implies that $A_n^{TE} = I_n^{TE}$ and $A_n^{TM} = I_n^{TM}$. Recalling the expressions for I_n^{TE} and I_n^{TM} in equation 46 as well as the expressions for the TE and TM electric field in equations 2 and 6, we confirm that in this special case ($k_{i,x} = 0$ and $E_i = E_0 \hat{x}$),

$$\begin{cases} A_n^{TE} = 0 \text{ for all } n \\ A_n^{TM} = \begin{cases} 0 & \text{for } n > 0 \\ \frac{E_0}{B_0 \omega} & \text{for } n = 0. \end{cases} \end{cases}\tag{51}$$

One can check that this solution satisfies the electric field continuity equation 38, as expected. For this case study, all of the power from the incoming wave couples into the TEM mode with 100% power transmission. No higher order modes are excited.

3 Simulations in HFSS

3.1 Simulation Methodology

For the more general case of an arbitrary plane wave and non-infinite waveguide geometry, it is beneficial to use electromagnetic wave simulation software to streamline the process of analyzing the incident plane wave, modeling its propagation, and determining its radiation pattern on the output side of the waveguide. We selected Ansys HFSS as the primary tool for our blackbody radiation simulations due to its strength in frequency-domain electromagnetic analysis. Our work focuses on steady-state power transmission, for which frequency-domain solvers provide superior accuracy and efficiency compared to time-domain approaches.²

The setup for the simulation is as follows:

- On the input side, a photon transitions from particle-like simulation in Geant4 to wave-like simulation in HFSS. The input parameters for the photon are its frequency, its input wavevector (parametrized by its input θ_{in} and ϕ_{in}), and its electric field polarization; see figure 3.
- On the output side, a photon transitions from wave-like simulation in HFSS to particle-like simulation in Geant4. The output parameters for the photon are the probability distribution over output locations on the output face of the waveguide, the probability distribution over output wavevectors emitted from the waveguide (parametrized by its output θ_{out} and ϕ_{out}), and the electric field polarization of the outgoing photon.

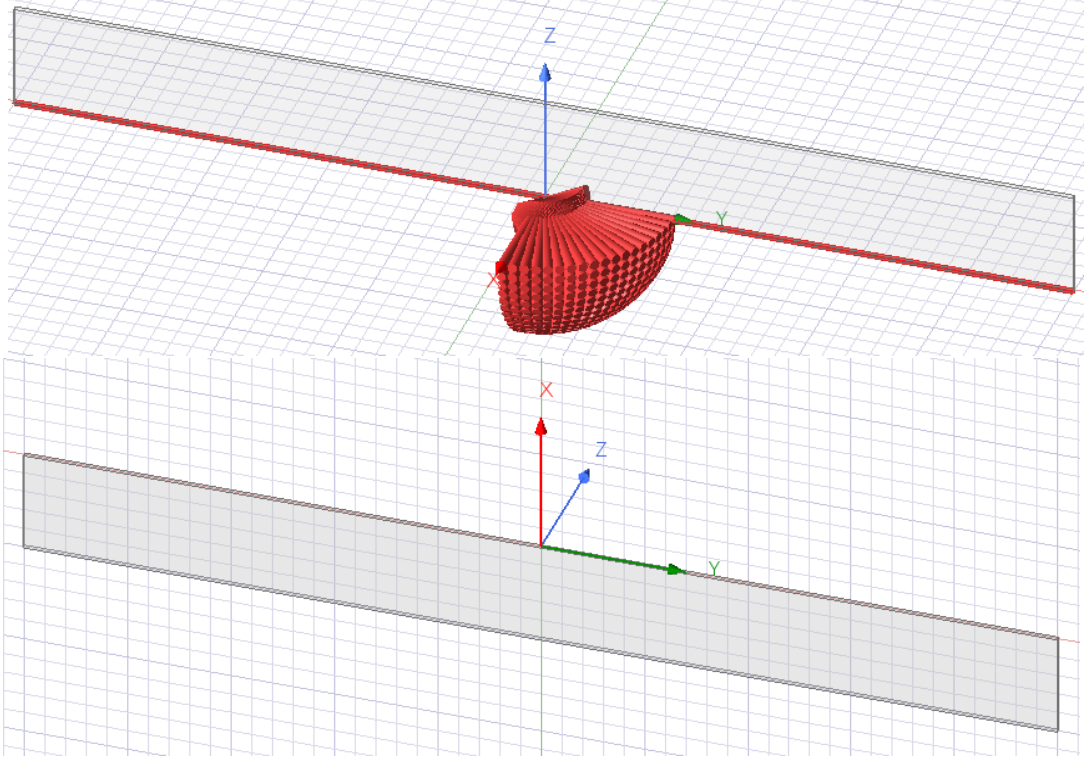


Figure 3: Top: Sweep over input angles, $90^\circ \leq \theta_{in} \leq 180^\circ$ and $0^\circ \leq \phi_{in} \leq 90^\circ$, at 2° angular fineness, for a waveguide axis in the $+\hat{z}$ direction. The direction of the (overlapping) arrows indicate the direction of the input wavevector. We constrain ϕ_{in} to a quarter-circle due to symmetry. HFSS is able to parametrically sweep over all such input angles and polarizations efficiently. To accurately model the entrance and exit of the waveguide into free space, we impose radiation boundary conditions on the input and output faces of the waveguide. The rest of the faces have perfect electric conductor (PEC) boundary conditions. Bottom: Different coordinate system defined at the outgoing face of the waveguide. The outgoing coordinate system has been redefined at the output face such that a sweep over ϕ_{out} corresponds to the sweep over the long rectangular dimension while the sweep over θ_{out} corresponds to the sweep over short rectangular dimension.

One benefit of separating the wave-like and particle-like nature of photons is that it becomes possible to precompute wave interactions using HFSS and store the results in a lookup table. We create a lookup table for every crack in the detector geometry. This approach allows us to simulate the full electromagnetic behavior of the system in advance without repeating costly full-wave simulations during every particle tracking run. Thus, even though the bulk of the photon simulation is carried out in Geant4, when a photon encounters a geometric feature such as a crack, slot, or waveguide, the simulation can quickly reference the corresponding HFSS-derived field solution from the lookup table. This hybrid method significantly speeds up the simulation while maintaining physical accuracy.

The mechanism for calculating the necessary output probability distributions is modularized over three steps.

- (i) Firstly, an incident plane wave is propagated through the waveguide via an incident plane wave excitation in HFSS. The time-averaged power incident on the waveguide can be calculated as

$$P_{in} = \int_I |\mathbf{S}_{in}| dA, \quad (52)$$

where \int_I refers to an integral over the outgoing face and $\mathbf{S}_{in} = \frac{1}{2} \frac{\mathbf{E} \times \mathbf{B}}{\mu_0}$ indicates the time-averaged Poynting vector of the incoming wave. Notice that in this case, we are not interested in the flux of the Poynting vector ($\int_I \mathbf{S}_{in} \cdot d\mathbf{A}$) through the input face, because the propagation of the wave is not necessarily aligned with the direction of the waveguide.

From the simulation, we obtain a value of the time-averaged transmitted power by integrating the Poynting vector \mathbf{S}_{out} over the outgoing face, i.e.

$$P_{out} = \int_O |\mathbf{S}_{out}| dA, \quad (53)$$

where \int_O refers to an integral over the input face. As for the input face, we are concerned not about the flux of the Poynting vector through the outgoing face but rather the total power coming out of the output face regardless of directionality. This is because photons leaving the waveguide reenter free space, and we wish to account for the full power carried away, even if it is not perfectly aligned with the waveguide axis.

For the first stage, then, the probability that the photon propagates to the other end of the waveguide without being reflected or absorbed is given as

$$|S_{21}|^2 = \frac{P_{out}}{P_{in}}, \quad (54)$$

where $|S_{21}|^2$ represents the forward transmission coefficient.

- (ii) Secondly, given that the photon arrives at the output face, the probability distribution of output locations on the output face to feed back to Geant4 is given by $P(x, y) \propto |\mathbf{E}(x, y)|^2$, i.e. the probability for the photon to be emitted from any given point on the output face is proportional to the electric field squared at that point. We use the complex magnitude squared of the electric field ($|\mathbf{E}(x, y)|^2 = |E_x|^2 + |E_y|^2 + |E_z|^2$, where $E_x, E_y, E_z \in \mathbb{C}$), rather than the magnitude squared of the instantaneous electric field ($|Re[\mathbf{E}(x, y)]|^2$) because we are interested in the time-averaged intensity of the electric field over the outgoing face independent of the phase of the wave. Then, the numerical probabilities can be calculated from the discretized electric field positions $\{(x_i, y_i)\}$ as

$$P(x, y) = \frac{|\mathbf{E}(x, y)|^2}{\sum_{(x_i, y_i)} |\mathbf{E}(x_i, y_i)|^2}. \quad (55)$$

- (iii) Thirdly, given that the photon arrives at the output face, the probability distribution of output wavevectors (parametrized by θ_{out} and ϕ_{out}) to feed back to Geant4 can be found by analyzing the far-field radiation pattern, which is calculated in HFSS as the Fourier transform of the electric field at the output face. We can then use the same method as equation 55, i.e. from the discretized output angles $\{(\theta_i, \phi_i)\}$ as

$$P(\theta, \phi) = \frac{|\mathbf{E}(\theta, \phi)|^2}{\sum_{(\theta_i, \phi_i)} |\mathbf{E}(\theta_i, \phi_i)|^2}. \quad (56)$$

where again $|\mathbf{E}(\theta, \phi)|^2$ denotes the complex magnitude squared of the far-field electric field at outgoing angles θ and ϕ . Given an outgoing angle parametrized by (θ, ϕ) , the polarization of the outgoing photon can be inferred through the far-field radiation pattern as well:

$$\hat{e}_{out} = \frac{\mathbf{E}(\theta, \phi)}{|\mathbf{E}(\theta, \phi)|}. \quad (57)$$

The main difficulty in creating these lookup tables lies in the need to evaluate many combinations of input parameters, including frequency, wavevector direction, and input electric field polarization. One simplification is to use symmetry to simulate only a subset of the possible input angles, as shown in figure 3. Another simplification is to simulate only two orthogonal polarization directions. We denote the two orthogonal directions by $\hat{\mathbf{E}}_\theta$ and $\hat{\mathbf{E}}_\phi$, where the unit vector in the θ direction is $(\cos \theta \cos \phi, \cos \theta \sin \phi, -\sin \theta)$, and the unit vector in the ϕ direction is $(-\sin \phi, \cos \phi, 0)$. A depiction of the two polarization states is given in figure 4. Results for any arbitrary polarization can then be reconstructed by linearly combining the outcomes from this basis due to linearity of Maxwell's equations. In particular, if the ingoing electric field polarization is $\hat{e}_{in} = E_\theta \hat{\mathbf{E}}_\theta + E_\phi \hat{\mathbf{E}}_\phi$, then $\mathbf{E}(x, y)$ and $\mathbf{E}(\theta, \phi)$ become

$$\begin{aligned} \mathbf{E}(x, y) &\rightarrow E_\theta \mathbf{E}_{E_\theta=1, E_\phi=0}(x, y) + E_\phi \mathbf{E}_{E_\theta=0, E_\phi=1}(x, y) \\ \mathbf{E}(\theta, \phi) &\rightarrow E_\theta \mathbf{E}_{E_\theta=1, E_\phi=0}(\theta, \phi) + E_\phi \mathbf{E}_{E_\theta=0, E_\phi=1}(\theta, \phi) \end{aligned} \quad (58)$$

where the subscripts on \mathbf{E} indicate one of the two orthogonal polarization directions. Equations 55, 56, and 57 then proceed as before with the replacements given in equation 58.

However, for each frequency and each of the two orthogonal polarization states, we must still compute the waveguide response across a range of incident and outgoing angles. A naive approach would be to uniformly sample the entire input and output angular space (in both θ and ϕ) at high resolution, but this quickly becomes computationally intractable. To make the problem more manageable, we must adopt simplifying assumptions or employ adaptive sampling strategies that focus computational resources on the most relevant or high-contrast regions of parameter space.

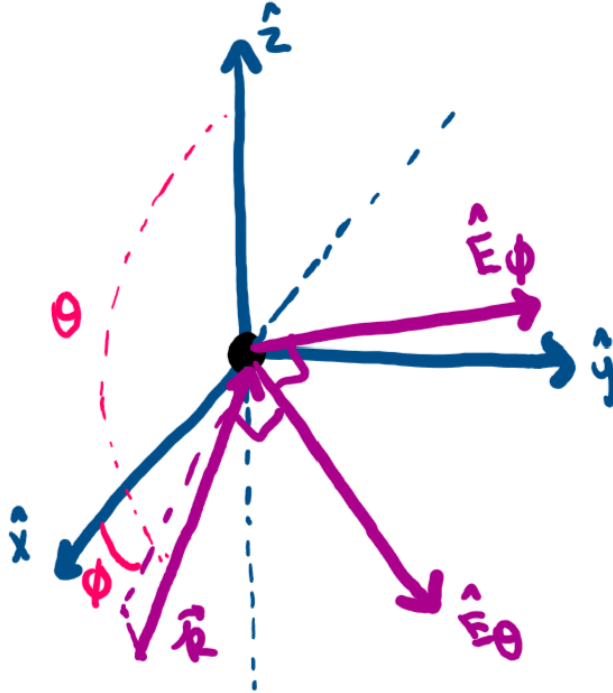


Figure 4: Incoming plane wave with wavevector \mathbf{k} , and the two orthogonal electric field polarization directions $\hat{\mathbf{E}}_\phi$ and $\hat{\mathbf{E}}_\theta$.

Firstly, we must decide how finely to sample the probability distribution over output angles θ_{out} and ϕ_{out} . The typical angular width of the main lobe when a wave passes through an object of characteristic lengths a and b is

$\phi_{diff} \sim \frac{\lambda}{a}$ and $\theta_{diff} \sim \frac{\lambda}{b}$. The characteristic lengths vary based on the geometry of the crack; for an infinitely large parallel-plate waveguide modeled as a long rectangular waveguide, the characteristic lengths are the side lengths. We sample a fineness of $\lambda/10a$ and $\lambda/10b$ to ensure finer coverage of the output patterns. By sampling at this fineness, we also ensure that the simulation does not miss small but significant side lobes in the diffraction pattern. Some examples of diffraction patterns are shown in figure 5.

Secondly, we find from the simulation data and see in figures 6 and 7 that both $|S_{21}|$ and the far-field radiation pattern are generally continuously and slowly varying functions of the input angles θ_{in} and ϕ_{in} . This means that in the simulation, it is possible to sample the input angles in a slightly coarser fashion and interpolate the intermediate values as necessary. We provide more details regarding the interpolation in section 3.3.

Of course, certain regions of input angles demand more precision than others, particularly those with a high derivative in output power and far-field radiation pattern. To this end, we apply an adaptive scheme to sampling input angles, employing an initial coarse sweep in θ_{in} and ϕ_{in} , finding the most important regions to refine (based on point-to-point difference in output power), and iteratively refining those regions. An example of this refinement scheme patching large gaps in the outgoing power is given in figure 8. The initial coarse sweep is in increments of 0.8° , a choice that is motivated later. The process terminates when the following criterion is met: for each pair of neighboring points in θ_{in} and ϕ_{in} , the point-to-point absolute difference in outgoing power is less than 1.5% of the power incident on the waveguide. The reason that the value of 1.5% is chosen is that it balances the precision needed before the interpolation process with the time required to run and export data from the HFSS simulation. We use absolute rather than relative point-to-point power differences in this refinement criterion. While relative differences can be more sensitive to small features such as side lobes, they tend to over-emphasize regions of low total power, where even small absolute variations produce large relative changes. In this particular case, we are interested in accurately capturing the total blackbody power transmitted through the waveguide, which is dominated by the main lobe. Small side lobes contribute negligibly to the integrated power and are not critical for our application. This contrasts with applications such as antenna pattern characterization or optical system alignment, where even low-power features like side lobes or interference fringes can carry critical information.

While the refinement criterion is based on outgoing power, we emphasize that the same smooth dependence on input angles θ_{in} and ϕ_{in} is also observed in the output far-field radiation pattern. Therefore, the adaptive scheme provides adequate angular resolution not just for power interpolation but also for accurately capturing directional emission characteristics. This convergence criterion also motivates the choice of the initial sampling interval. If we assume the output power varies sinusoidally with angle, its derivative is bounded by unity. Therefore, over a 0.8° interval, the maximum possible change in outgoing power as a fraction of the incoming power should be around 1.4%, which is below our 1.5% refinement threshold. Thus, an initial 0.8° sweep serves as a principled starting point for the adaptive procedure. Naturally, regions with more rapid angular variation will be automatically refined further during subsequent iterations.

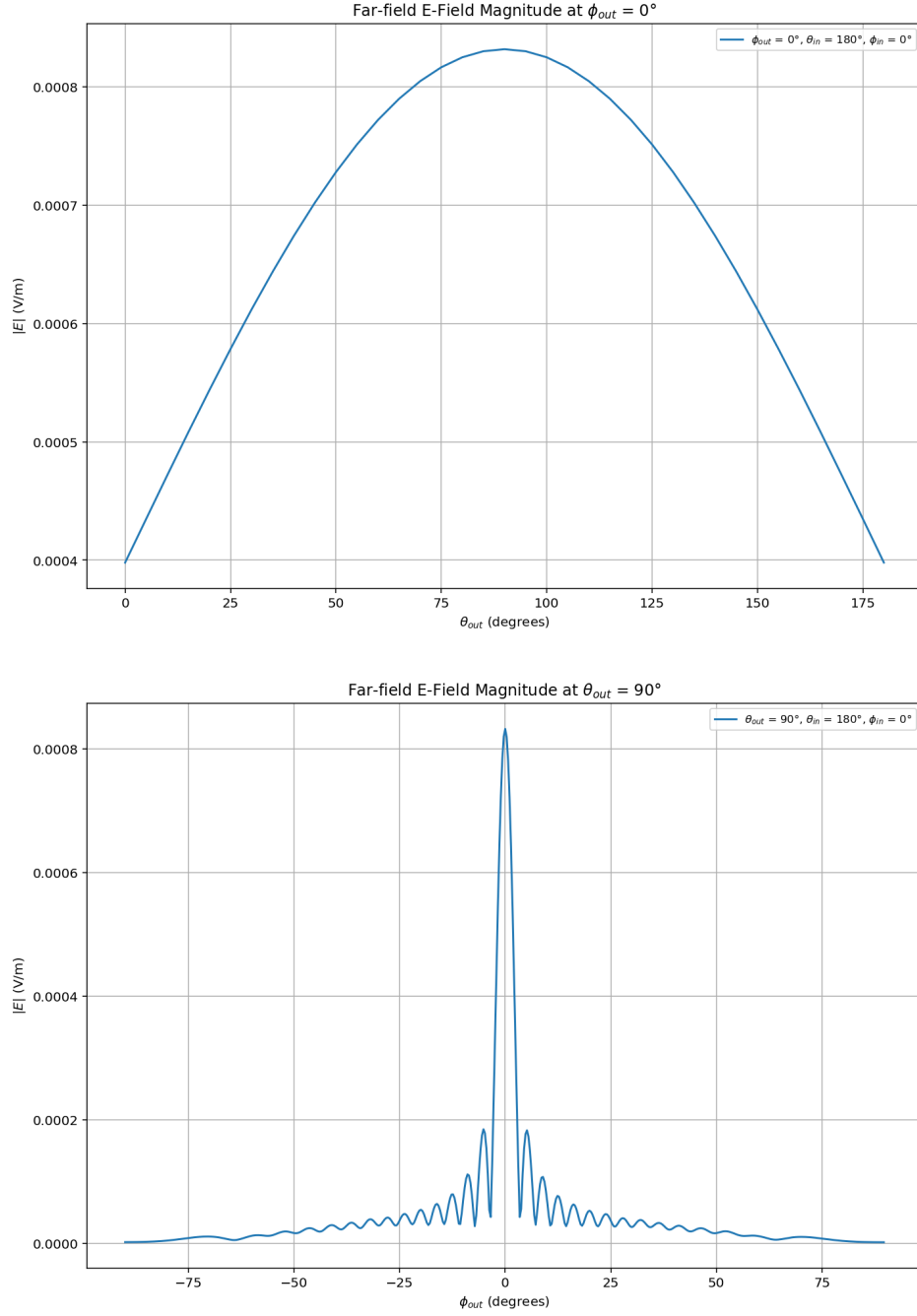


Figure 5: Variations in the far-field electric field as a function of θ_{out} and ϕ_{out} , for $\theta_{in} = 180^\circ$, $\phi_{in} = 0^\circ$, $E_\phi = 0$, $E_\theta = 1$, $f = 500\text{GHz}$, and rectangular waveguide dimensions $a = 10\text{mm}$ and $b = 0.05\text{mm}$. Top: Far-field electric field variations as a function of θ_{out} for $\phi_{out} = 0^\circ$. We see a relatively wide diffraction pattern. Bottom: Far-field electric field variations as a function of ϕ_{out} for $\theta_{out} = 90^\circ$. We see a finely sampled diffraction pattern with relatively narrow structures. The widths of both diffraction patterns are consistent with $\phi_{diff} \sim \frac{\lambda}{a}$ and $\theta_{diff} \sim \frac{\lambda}{b}$.

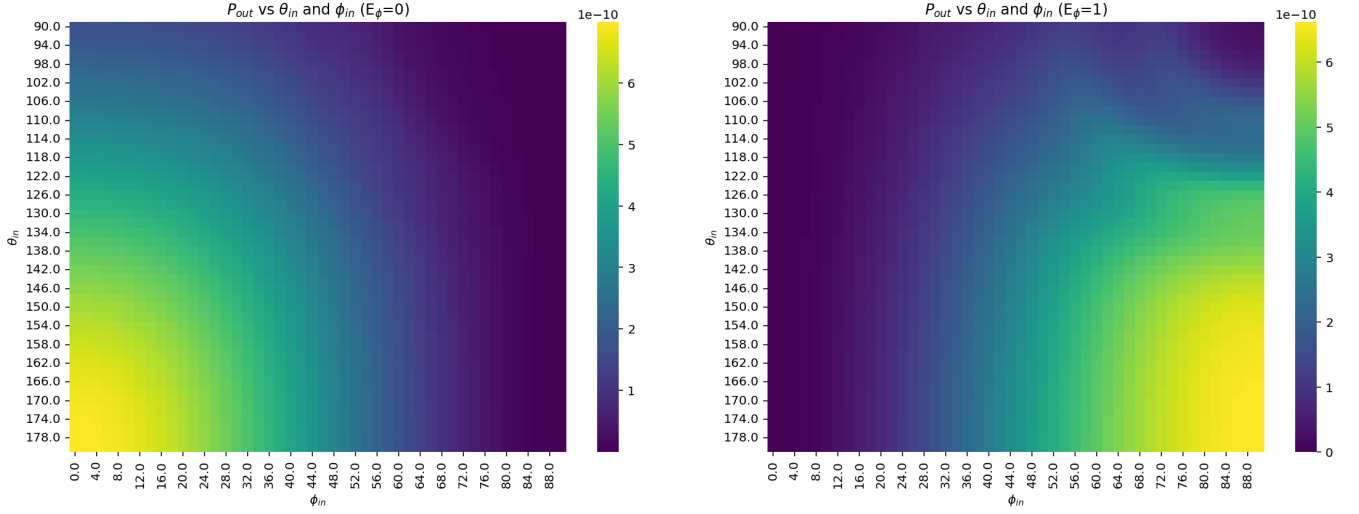


Figure 6: Outgoing power P_{out} as a function of the incoming angles θ_{in} and ϕ_{in} , for $f = 500\text{GHz}$ and rectangular waveguide dimensions $a = 10\text{mm}$ and $b = 0.05\text{mm}$. The convention for the coordinate system of the input angles is based on figure 3. Left: $E_\phi = 0$, $E_\theta = 1$. Right: $E_\phi = 1$, $E_\theta = 0$. Notice in both cases that the outgoing power is a smoothly varying function of the input angles. Here, the angular resolution is 2° in the input angles.

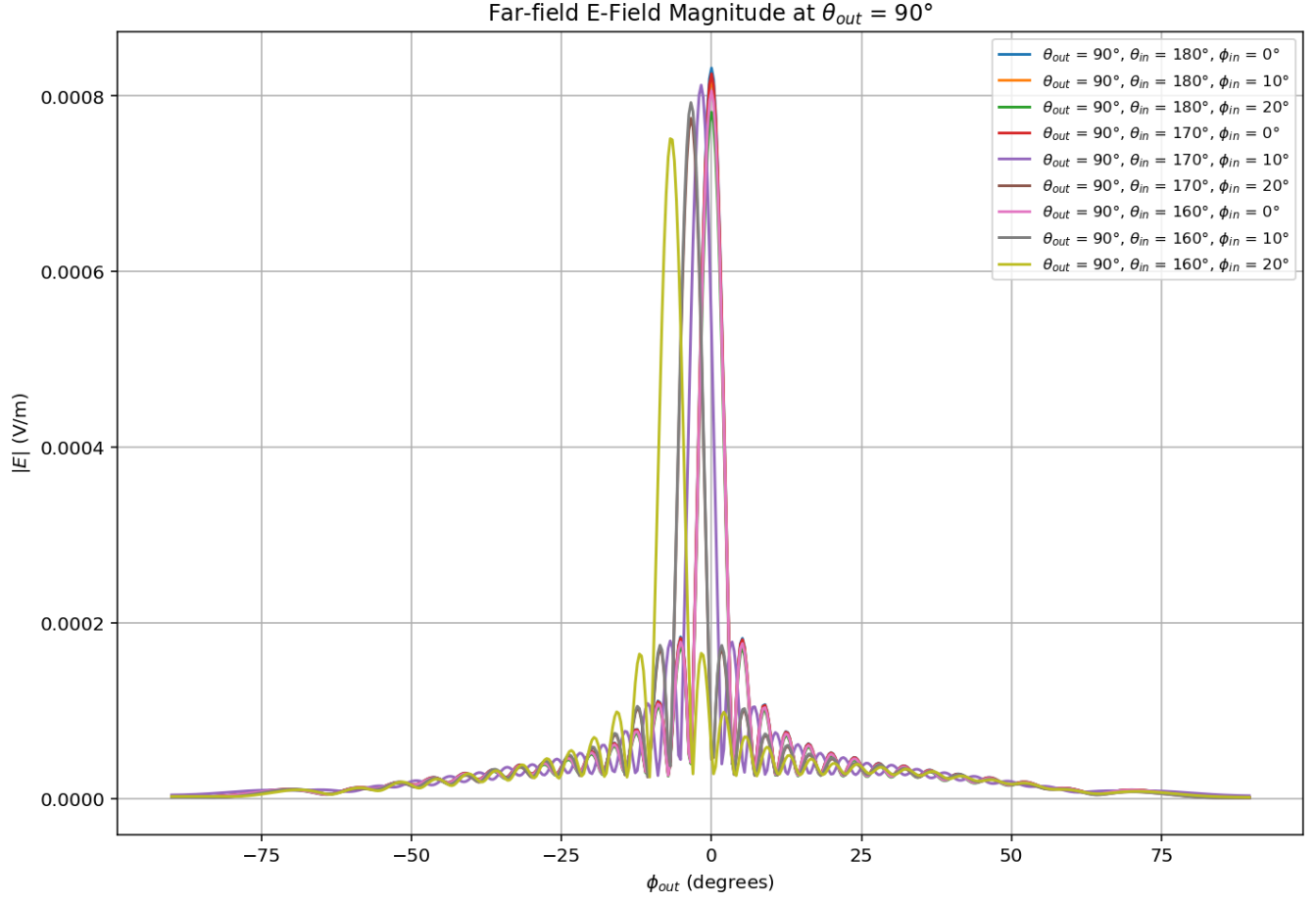


Figure 7: Variations in the far-field electric field as a function of ϕ_{out} for $\theta_{in} \in \{160^\circ, 170^\circ, 180^\circ\}$ and $\phi_{in} \in \{0^\circ, 10^\circ, 20^\circ\}$, for a total of 9 combinations. The convention for the coordinate system for the angles is the same as in figure 3. The static parameters are $\theta_{out} = 90^\circ$, $E_\phi = 0$, and $E_\theta = 1$. We see the slow and continuous dependence of the pattern on input angles θ_{in} and ϕ_{in} , which allows for interpolation.

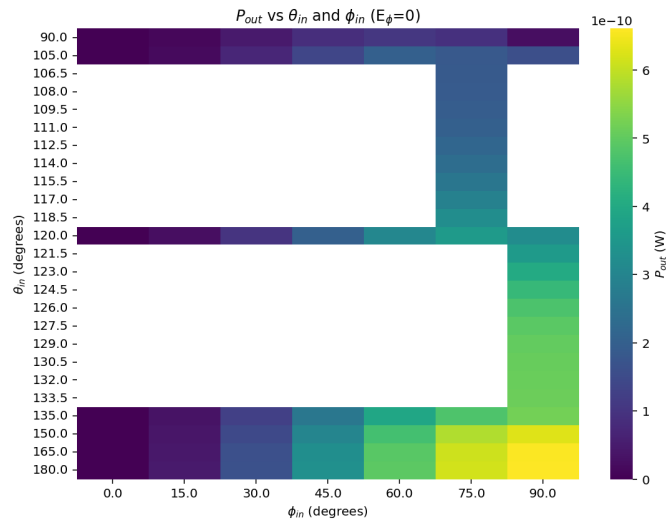


Figure 8: Illustration of the adaptive sweep: large jumps in the outgoing power between $(\phi, \theta) = (75^\circ, 120^\circ)$ and $(75^\circ, 105^\circ)$ are patched. Similar, large jumps in the outgoing power between $(\phi, \theta) = (90^\circ, 135^\circ)$ and $(90^\circ, 120^\circ)$ are patched.

In order to further speed up the simulation, High-Performance Computing (HPC) can be used to run different frequencies in parallel. HPC does not reduce the runtime for a single frequency, but by running multiple frequencies in parallel, it shortens the total wall-clock time for the full sweep to a practical level.

Finally, for each frequency and polarization, the refined data file is output as a .csv file. The probability distribution governed by this data can then be randomly sampled to determine the output wavevector for the incoming photon. The HFSS lookup table component of the simulation can thus be treated as a scattering problem, in which the incoming photon is probabilistically scattered to a new output location with a new wavevector and polarization. After exiting the waveguide geometry, the photon then proceeds in a particle-like manner modeled in Geant4.

3.2 Different Geometries

We have thus far discussed the numerical HFSS simulations in the context of a rectangular waveguide with dimensions a and b , but in fact the conclusions derived from the case of the rectangular crack geometry can be extended to more general crack geometries.

Cylindrical Waveguide; Height-perturbed Waveguide; Right-angle Waveguide We also analyzed how the outgoing power and far-field radiation pattern vary with the input angle for three different geometries: a cylindrical waveguide, a height-perturbed waveguide, and a right-angle waveguide, as illustrated in figure 9. In all cases, we observed a smooth dependence on the input angle for both the outgoing power and the far-field electric field. While the cylindrical waveguide exhibits two-dimensional symmetry, the height-perturbed and right-angle waveguides do not. The continued smoothness of the system’s response, even in the absence of symmetry, is especially promising for interpolation-based approaches. For brevity, we present only the results for the right-angle waveguide in figure 10. Due to the presence of the TEM mode, the results are remarkably similar to figures 6 and 7.

The effects of height perturbations and right-angle turns have been previously examined by Chang² in the context of blackbody radiation. The study concluded that dominant TEM mode propagation is largely unaffected by these structural variations. Since the TEM mode lacks a cutoff frequency, additional strategies are required to suppress its propagation and effectively mitigate blackbody radiation.

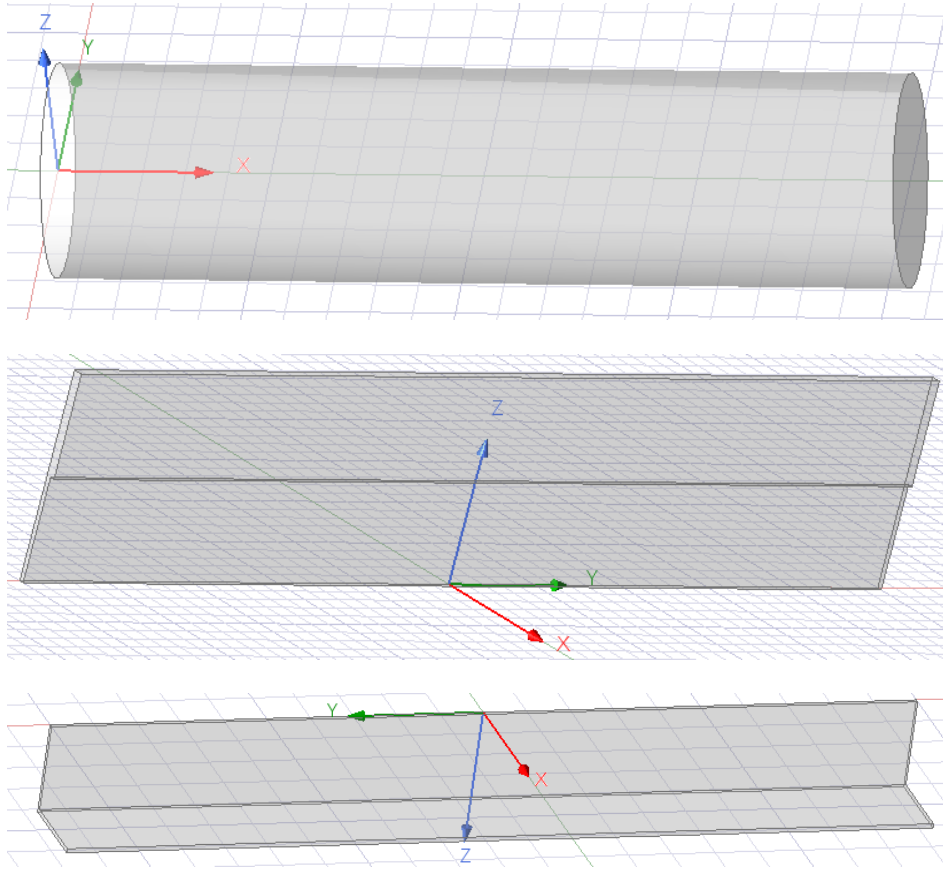


Figure 9: Additional prototype geometries for the HFSS simulation. Top: Cylindrical waveguide. Middle: Height-perturbed waveguide. Bottom: Right-angle waveguide.

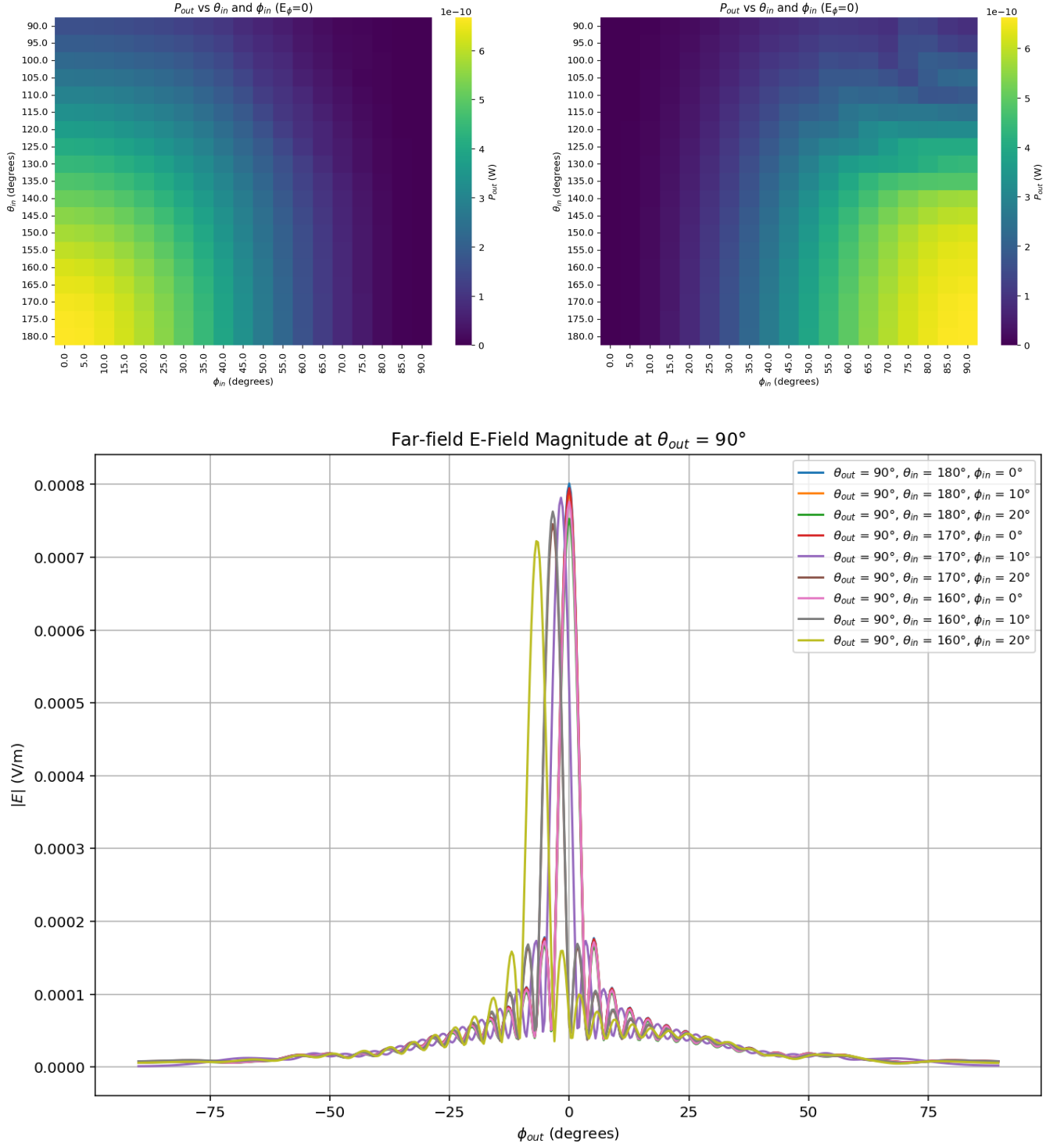


Figure 10: Top: Plots analogous to figure 6 for the case of the right-angle waveguide. The ingoing and outgoing coordinate systems are the same, given in figure 9. Here, the angular resolution is 5° in the input angles. Bottom: Plots analogous to figure 7 for the case of the right-angle waveguide. The static parameters are $\theta_{out} = 90^\circ$, $E_\phi = 0$, and $E_\theta = 1$. The smooth dependence on the input angles allows for interpolation of the results.

Optimal Labyrinth One possible photon-shielding strategy, first proposed by Chang,² is the labyrinth shown in figure 11. The design introduces wide intermediate sections within the waveguide to scatter blackbody radiation into non-TEM modes. In particular, the 500 μm high section immediately following the entrance induces non-TEM

transmission, while the subsequent 100 μm and 200 μm sections qualitatively represent machining tolerances from a sliding fit. Compared to a purely TEM-propagating reference model, this geometry enhances shielding of blackbody radiation in the frequency range between DC and the first cutoff of the higher-order modes.

Despite the complexity of the geometry, we found that varying the incoming angles did not drastically shift the transmitted power or the far-field electric field pattern. Rather, the dependence on incoming angles remains relatively smooth, even though the far-field pattern itself becomes more complex, as shown in figure 12. We also see that the magnitude of the far-field electric field in the case of this labyrinth is smaller than the magnitude of the far-field electric field in other designs, which indicates that less power is transmitted through the labyrinth compared to a standard rectangular waveguide.

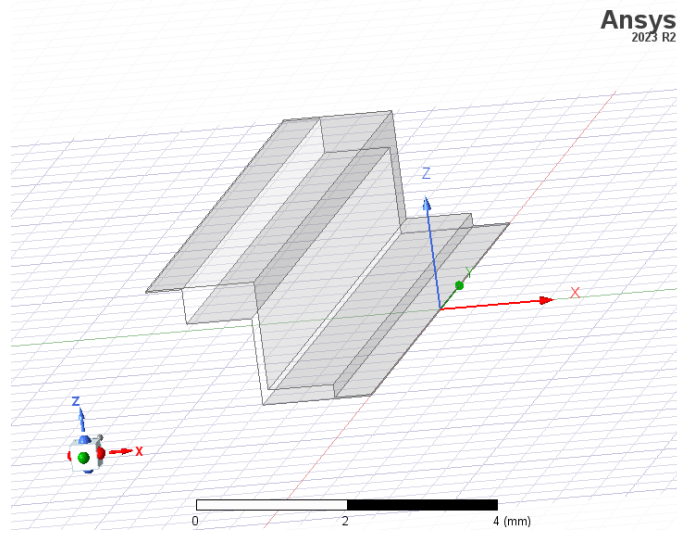


Figure 11: The optimal labyrinth, first proposed by Chang.² The coordinate system depicted is the outgoing coordinate system, where the scattered wave exists the waveguide.

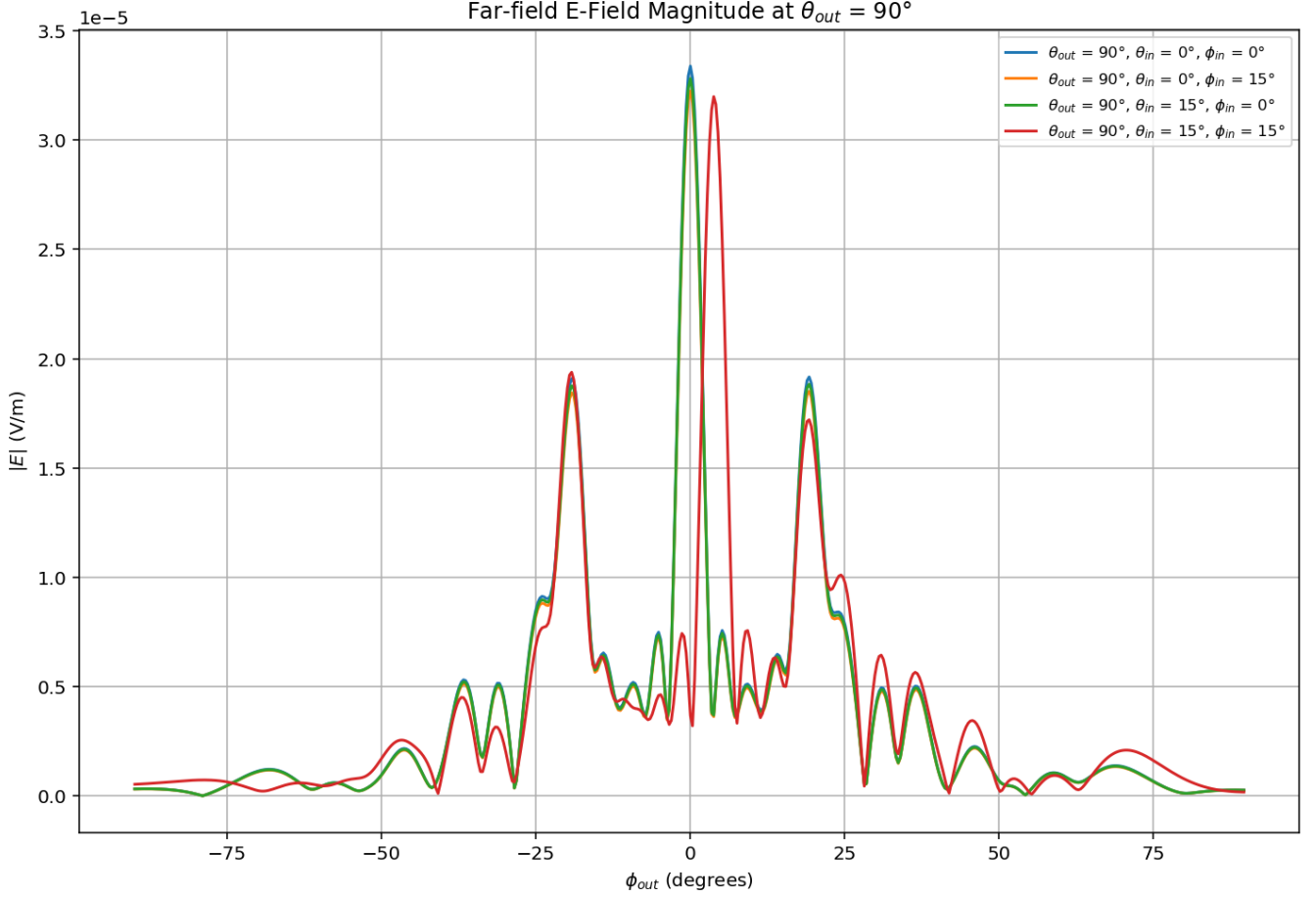


Figure 12: Variations in the far-field electric field as ingoing angles are varied. The magnitude of the electric field is diminished compared to figure 7, indicating effective blockage of blackbody radiation. The dependence on the ingoing angles is seen to be smooth.

Stub Filter As a final example geometry, another blackbody radiation mitigation strategy suggested by Chang was the idea of adding waveguide stub filters. A waveguide stub filter consists of one or more short sections of waveguide, called stubs, connected perpendicularly to the main waveguide and terminated with a PEC (short-circuit).

One can define the guided wavelength to be

$$\lambda_g = \frac{\lambda}{\sqrt{1 - \left(\frac{\lambda}{\lambda_c}\right)^2}}, \quad (59)$$

where λ is the free-space wavelength corresponding to a given frequency and λ_c is the cutoff frequency of the waveguide. The guided wavelength represents the wavelength of an electromagnetic wave as it actually propagates through a guiding structure. If the stubs are $\lambda_g/4$ long, the structure functions as a band-stop filter, with each stub behaving like a parallel resonant circuit in series with the waveguide. If the stubs are $\lambda_g/2$ long, the filter becomes a band-pass type, and each stub resembles a series LC resonant circuit also in series with the waveguide.⁶

We simulated the response of the waveguide to both $l = \lambda_g/4$ and $l = \lambda_g/2$ stubs at $f = 500\text{GHz}$. The cutoff frequency for the parallel plate waveguide is essentially $f_c = 0$, or $\lambda_c = \infty$, and so $\lambda_g \approx \lambda \approx 600\mu\text{m}$. For this frequency, the plots of the magnitude of the complex electric field are shown in figure 13. The results are consistent with expectations, providing further evidence for the validity of the simulation.

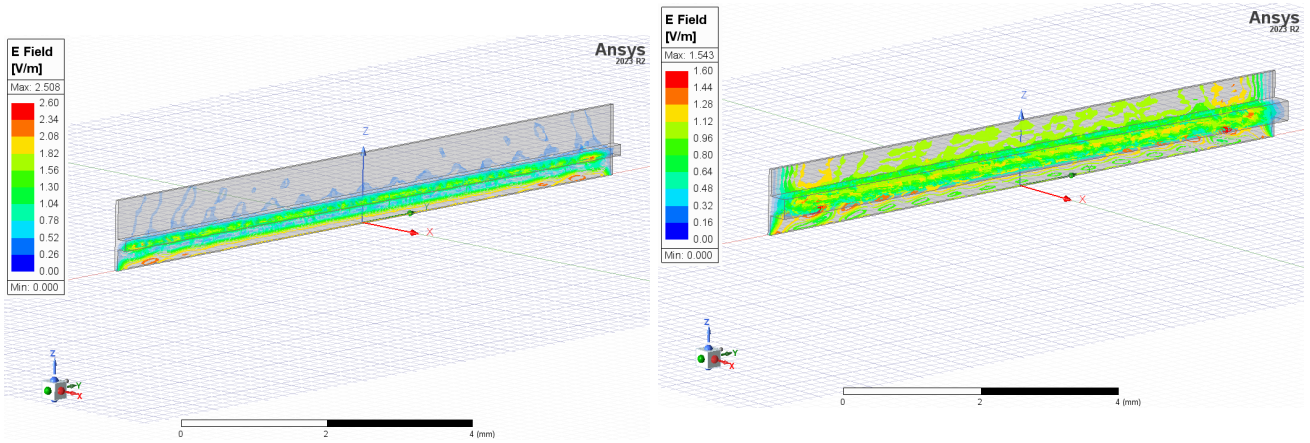


Figure 13: Magnitude of the complex electric field in the stub-filter waveguide at $f = 500\text{GHz}$. Left: Band-stop filter with stub length $l = \lambda_g/4 \approx 150\mu\text{m}$. Right: Band-pass filter with stub length $l = \lambda_g/2 \approx 300\mu\text{m}$. We see that the power transmission for the band-stop filter is much lower than for the band-pass filter. Quantitatively, $|S_{21}|^2 = 0.04$ for the band-stop filter and $|S_{21}|^2 \approx 1$ for the band-pass filter.

3.3 Interpolation

Finally, let us discuss methods for interpolating simulation data for reintroduction into Geant4. The electromagnetic outputs – scalar transmission coefficient $|S_{21}|^2$, complex electric field at the outgoing face, and far-field electric field – are sampled over a multi-dimensional parameter space of frequency, input and output angles, and spatial coordinates. For each of the two orthogonal polarization directions, the input parameters and corresponding outputs of the three relevant quantities are shown in table 1.

Quantity	Input Variables	Output Variables
$ S_{21} ^2$	$f, \theta_{in}, \phi_{in}$	$ S_{21} ^2(f, \theta_{in}, \phi_{in})$
E-field at Exit Face	$f, \theta_{in}, \phi_{in}, x, y, z$	$\mathbf{E}(f, \theta_{in}, \phi_{in}, x, y, z)$
Far-field E-field	$f, \theta_{in}, \phi_{in}, \theta_{out}, \phi_{out}$	$\mathbf{E}(f, \theta_{in}, \phi_{in}, \theta_{out}, \phi_{out})$

Table 1: Input and output variables for the three quantities of interest. The output variables directly correspond to the probability distributions described in section 3.1, so this table describes the input and output variables of the desired lookup table.

Classical approaches such as radial basis function interpolation, tensor-product splines, and kriging provide smooth, physically consistent estimates but can be computationally expensive for large datasets. Reduced-order modeling mitigates this by projecting the fields onto a small set of modal basis functions (e.g., waveguide or spherical harmonics) and interpolating only the modal coefficients. A particularly effective strategy combines this with machine learning: the fields are first compressed via proper orthogonal decomposition (POD) into parameter-independent, dominant modes, and neural networks are trained to map input parameters (frequency, angles, and spatial coordinates) to the corresponding modal coefficients.⁷ The full fields can then be efficiently reconstructed from these coefficients, yielding smooth, accurate, and physically consistent predictions across the multi-dimensional parameter space. Once the fields are obtained, they can be sampled from as described section 3.1.

4 Discussion

Our work in this paper provides an important intermediate step in the full, end-to-end modeling of blackbody radiation in cryogenic, dark matter detectors. Ultimately, accurately modeling the propagation of blackbody radiation through various non-hermeticities in fridge geometries will serve an important role in understanding the magnitude and severity of blackbody radiation-induced leakage currents and parasitic power on CDMS detectors.

Returning to the larger picture of modeling blackbody radiation in both open and bounded space conditions, the process is as follows. The fridge geometry is modeled in Geant4, where photons are spontaneously created through thermal surfaces. The photon spends a majority of its lifetime in open space conditions, where the characteristic

length of the space is larger than the wavelength of the photon. However, whenever the photon encounters the boundary between an open space and a bounded space, the lookup table generated for that particular crack geometry is quickly consulted to determine the probability of transmission through the crack, the probability distribution of the photon's emission location, and the outgoing probability distribution of the photon's outgoing wavevector. These probability distributions are then sampled, and the photon is returned to the Geant4 simulation with these properties. Thus, the HFSS, bounded space simulation builds an important bridge between open space simulations in HFSS.

Although we have made significant progress in creating the simulations, there remain improvements that may be implemented in the future. For a 0.8° input sweep coarseness and a 1.5% point-to-point absolute difference in outgoing power on a simple rectangular waveguide geometry, the full adaptive sweep takes ~ 1 day to run for a given frequency. Since we are mainly interested in propagation of thermally-generated photons ranging from temperatures between 3K and 300K, corresponding to peak frequency emissions of 180GHz and 18THz via Wien's law, our frequency sweep needs to span two orders of magnitude. Because the dependence of the outgoing power and far-field electric field on frequency is smooth (see figure 14), we adopt a logarithmic sweep with approximately 10% point-to-point frequency steps, which provides sufficient sampling for accurate interpolation. Over two orders of magnitude, this requires ~ 50 frequencies to be sampled for each crack geometry. Given the computational cost of each frequency point, such a sweep becomes prohibitively time-consuming on a single workstation. Future work will therefore require access to high-performance computing resources, where parallelization across frequencies and geometries can reduce turnaround time from weeks to days. Because each crack geometry need only be sampled once, a multi-day runtime per geometry is acceptable.

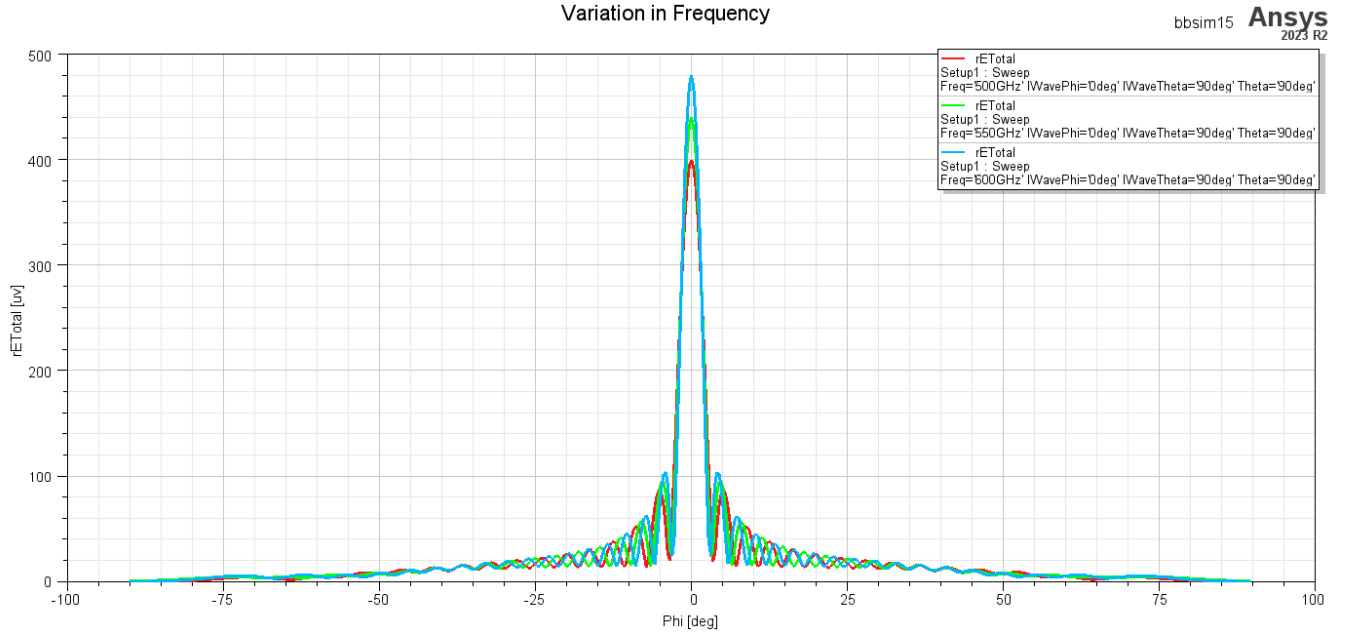


Figure 14: Variations in the far-field electric field as a function of frequency, for $\theta_{in} = 180^\circ$, $\phi_{in} = 0^\circ$, $E_\phi = 0$, $E_\theta = 1$, $f = 500\text{GHz}$, and rectangular waveguide dimensions $a = 10\text{mm}$ and $b = 0.05\text{mm}$. We see that for 10% changes in frequency, the dependence of the outgoing radiation pattern changes in a smooth and predictable manner.

In the future, it will also be prudent to test the simulation in two different ways. Firstly, future work may build on the analytical solution to the infinite parallel-plate waveguide, which can be thoroughly tested and compared to the HFSS simulation developed. Secondly, the modeling may be extended to the actual geometry of a dilution refrigerator from SLAC, allowing us to test how cracks behave in a realistic experimental environment. Such a study would directly inform the applicability of our simulation. Finally, by combining the Geant4 and HFSS components of the photon lifetime, we can compare the influence of blackbody radiation against theoretical predictions made for the SLAC fridges.

The blackbody simulations presented may also shed light on future mitigation techniques to counteract blackbody radiation-induced leakage currents, such as exploiting waveguide cutoff frequencies through precisely machined narrow gaps, minimizing seal entrance areas, and introducing widened sections to scatter TEM radiation into higher-

order modes that can be more effectively attenuated downstream.²

Together, these simulations offer a pathway toward end-to-end modeling of thermally generated photons, enabling both accurate prediction of blackbody-induced effects and the development of practical mitigation strategies for future dark matter experiments.

Acknowledgements

Firstly, I would like to extend my sincere thanks to my mentor, Professor Sunil Golwala, for his invaluable insights and advice in both the analytical and simulation aspects of this work, as well as his guidance throughout the project. I appreciate your willingness to answer questions and offer meaningful suggestions at times when progress was difficult.

I would also like to thank Yen-Yung Chang for being consistently available to answer questions, assisting with the analytical derivation, and providing suggestions for HFSS simulations. Much of the HFSS methodology in this work was inspired by his paper, and his guidance was invaluable throughout the project.

I would further like to thank Rohan Shenoy for his contributions to the Geant4 component of the blackbody simulations and for providing helpful suggestions on HFSS-related issues. Additionally, I thank Robin Xiong for offering thoughtful feedback that helped improve the overall quality of the simulations.

I want to express my heartfelt thanks to my friends Hailey Hartman, Kenji Farrell, Nikash Gupta, Shreyas Singh, and Warren Zhang for their unwavering support and encouragement throughout the project. I am especially grateful to my father, whose guidance, encouragement, and steadfast belief in me have been a constant source of motivation.

Finally, I would like to thank the Ph 11 program and Richard G. Brewer for their generous funding and support, which made this project possible.

A Code

The full code for the blackbody simulations can be found in the following Github repository:

<https://github.com/ModerJason/Blackbody-Simulations/tree/main>

References

- [1] J. Domange et al. Thermally-stimulated current investigation of dopant-related d^- and a^+ trap centers in germanium for cryogenic detector applications. *Journal of Low Temperature Physics*, 167, 2012.
- [2] Yen-Yung Chang. *SuperCDMS HVeV Run 2 Low-Mass Dark Matter Search, Highly Multiplexed Phonon-Mediated Particle Detector with Kinetic Inductance Detector, and the Blackbody Radiation in Cryogenic Experiments*. Dissertation (ph.d.), California Institute of Technology, Pasadena, CA, 2023.
- [3] H. M. Noh and P. H. Pathak. A high frequency analysis of electromagnetic plane wave scattering. NASA Contractor Report NASA-CR-179759, NASA (National Aeronautics and Space Administration), September 1986. Also published as NAS 1.26:179759; TR-715723-1. Document ID: 19860023128.
- [4] Robert E. Collin. *Field Theory of Guided Waves*. McGraw-Hill Book Co., New York, 1960.
- [5] S. Koshikawa, Dilek Colak, Ayhan Altintas, K. Kobayashi, and Alexander Nosich. A comparative study of rcs predictions of canonical rectangular and circular cavities with double-layer material loading. *IEICE Transactions on Electronics*, E-80C:1457–1465, 11 1997.
- [6] George L. Matthaei, Leo Young, and E. M. T. Jones. *Microwave Filters, Impedance-Matching Networks, and Coupling Structures*. McGraw-Hill, 1964.
- [7] Philipp Weder, Mariella Kast, Fernando Henríquez, and Jan S. Hesthaven. Galerkin neural network-pod for acoustic and electromagnetic wave propagation in parametric domains, 2024.